



Analytical model for planar tube hydroforming: Prediction of formed shape, corner fill, wall thinning, and forming pressure

Chen Yang, Gracious Ngaile*

Department of Mechanical and Aerospace Engineering, North Carolina State University, Campus Box 7910, Raleigh, NC 27695, USA

ARTICLE INFO

Article history:

Received 18 October 2007

Received in revised form

21 April 2008

Accepted 25 May 2008

Available online 3 July 2008

Keywords:

Tube hydroforming

Closed-form solution

Finite element

ABSTRACT

An analytical model for planar tube hydroforming based on deformation theory has been developed. This analytical model can be used to predict hydroformed shape, corner fill, wall thinning, and forming pressure. As the model is based on a mechanistic approach with bending effects included, local strain and stress distribution across the wall thickness can be determined. This includes strain and stress distributions for the outer layer, inside layer, and middle layer. The model is validated using finite element analysis and tube hydroforming experiments on irregular triangular, irregular quadrilateral, and pentagonal hydroformed shapes.

© 2008 Elsevier Ltd. All rights reserved.

1. Introduction

Advances in numerical modeling have made possible reduction of experimentation on the design of various metal-forming processes such as forging, stamping, rolling, and tube hydroforming (THF). Finite element analysis (FEA) has been found to be a very useful tool in developing a progression sequence for sheet metal forming and forging. It has also been found that optimal/workable solution sequences can be narrowed very quickly by combining finite element (FE) simulations and expertise from experienced process designers [1]. One of the limitations of most of the current FE solution schemes for metal forming is that they do not provide parametric analysis; hence any parametric investigation is usually done manually by changing one FEA model to another until a feasible solution is obtained.

With classical metal-forming processes such as forging and stamping, there are various mathematical models that allow one to quickly determine parameters of interest for the specific process that will guide the modeler to initially set an FEA model that may be close to a workable solution. This is, however, not the case for THF, as this process is relatively new. Furthermore, there is less experience accumulated in the design of THF processes as compared to the classical metal-forming processes. Lately, FEA has been widely used in the development of THF processes. A lot of effort has been put in studying process variables for developing loading paths via FEA, etc. [2–9]. Although the advances in FEA capability have increased the utilization of this technology, more

research is needed to establish analytical models for THF. Establishment of closed-form analytical solutions for THF may help in understanding the mechanics behind the THF processes better. Analytic solutions facilitate parametric study and can aid an FEA modeler in seeking out optimal THF process conditions. The analytic solution exposes the underlying relationship between the variables, which may otherwise be obscured by numerical analysis.

Some of the analytical models and numerical studies using FEA for THF are briefly summarized below. Earlier work on analytical models was carried out by Asnafi [10] in 1999, where he derived relationships for axial forces, yield strength, limiting strength, friction, etc. In 2001, Xia [11] derived an analytical model to predict bursting and wrinkling failures for the expansion of circular tubes using internal pressure and end feeding. In 2002, Koc and Altan [12] applied plasticity, membrane, and thin-thick walled tube theories to predict buckling, wrinkling, and bursting as well as axial force, internal pressure, counter force, and thinning in THF. Other analytical models for tube failure have been discussed by several researchers [13,14]. In an attempt to determine the increase in formability of THF via dual hydroforming techniques, Jain et al. [15] derived plastic instability criteria for hydroforming of a bulged shape with external pressure. They found some increase in formability with dual hydroforming.

Rama et al. [16] developed a two-dimensional (2D) numerical method based on the membrane analogy to tube-sheet deformation with the concept of FEs for sheet discretization, while utilizing a kinematically admissible approach to derive explicit expressions for relating loads and deformation. Their results demonstrated that the formulation is computationally efficient

* Corresponding author.

E-mail address: gracious_ngaile@ncsu.edu (G. Ngaile).

Nomenclature

F_h	hoop force
P	internal pressure
r	outer radius
rr	corner radius
L	length of linear section
t	deformed tube thickness
t_0	initial tube thickness
K	strength coefficient

n	strain hardening coefficient
$\bar{\sigma}$	effective stress
$\bar{\epsilon}$	effective strain
μ	friction coefficient
$\sigma_\theta, \sigma_{\theta,o}, \sigma_{\theta,i}$	hoop stress
$\sigma_r, \sigma_{r,o}, \sigma_{r,i}$	radial stress
$\sigma_z, \sigma_{z,o}, \sigma_{z,i}$	longitudinal stress
$\epsilon_\theta, \epsilon_{\theta,o}, \epsilon_{\theta,i}$	hoop strain
$\epsilon_r, \epsilon_{r,o}, \epsilon_{r,i}$	radial strain
$\epsilon_z, \epsilon_{z,o}, \epsilon_{z,i}$	longitudinal strain

and can be a great tool for a process designer to study process feasibility. Characteristics of corner fill using a square die have been investigated by many researchers via FEA and analysis [17–19]. Hwang and Chen [20,21] developed a mathematical model to analyze tube expansion in a rectangular die with sticking friction condition and a square cross-section die with sliding friction condition. In 2007, Orban and Hu [22] developed an analytical model to study the friction characteristic of corner fill in planar THF with frictionless, sliding, and sticking friction conditions. All these incrementally analytical models provided effective ways and powerful tools to predict forming pressure, tube-thinning distribution, and friction characteristic of corner fill in planar THF, despite the limitations of the prescribed friction conditions and omission of bending effects.

In order to reduce the computational time associated with three-dimensional (3D)-FEA modeling of bend–stretch forming of rectangular tube sections, Miller et al. [23,24] developed a 2D analytical model which can capture the effect of tension, pressure, and loading history on the quality of the tubes. The model was based on the assumption that the problem variables do not change along the length. The results from this model were in good agreement with experimental results, implying that the 2D analytical model can be an efficient tool for parametric study of the forming process at the design stage. Corona [25] extended this model to be applicable for arbitrary tube cross-sections. Using this model they were able to run algorithm in the order of 2 min using a SUN Ultra-10 workstation. Based on the work of Miller et al. [24] and Corona [25], Guan et al. [27] proposed a Fourier-series-based FEA of THF for axisymmetric model and Guan and Pourboghraat discussed generalized plane strain model in [26]. Fourier interpolation functions were used in their models due to the fact that these functions lead to considerable reduction in the size of global stiffness matrix as well as the number of variables. In their generalized plane strain model, axial feeding was simulated by specifying compressive load or actual strain. Smith et al. [28] and Smith and Sun [29] introduced closed-form formulas for planar THF analysis. The formulae proposed could be used to predict the smallest achievable corner-fill radii and their corresponding forming pressure. Even though these formulae were derived on purely geometric analysis and assumed sticking friction conditions, the results agreed very well with experimental data for square section hydroformed parts. The formula derived by Smith et al. [28] and Smith and Sun [29] can benefit hydroforming process designers substantially in the early stages for determining feasibility of THF before embarking into extensive FE simulation, where more details on material flow, etc., could be obtained.

The present work introduces a mechanics-based analytical model for planar THF of both irregular and regular polygon shapes. This model employs total deformation theory, where the tool–tube interface friction is governed by Coulomb's friction law. The analytical model also includes bending effects of the deformed tube.

2. Objectives

In an attempt to understand the interrelationship of variables pertaining to analytical modeling of THF better, this paper will present mechanics-based derivation equations for a family of planar THF shapes. The derived equations are aimed at predicting the forming pressure, formed shape, corner fill, and wall thinning for regular and irregular polygon shapes. It is expected that this model may be beneficial in preliminary determination of the feasibility of hydroforming a part. The model is also expected to open new avenues for further derivation of analytical solutions that may incorporate different material models and also for extension to more sophisticated geometries. Since the derivation is based purely on mechanics, the analytical solutions also provide principal stresses and strains.

3. Plane strain THF analysis of polygon shapes

3.1. Scheme of analysis

We first present a family of irregular and regular polygon shapes showing the geometric constraints considered in the analysis. Figs. 1(a) and (b) show triangular, quadrilateral, and pentagon shapes before and after hydroforming has taken place. For each die set and tubular material, the following geometrical variables are given: part corner radius r , die corner angle α , and die–tube contact length L (Fig. 2).

As seen in Fig. 2, initially the tube will be in contact at the four points N1, N2, N3, and N4. As the tube expands, line contact will start forming in four regions for the case of a quadrilateral. At a process time tp , contact length Li will be formed in the four regions. The contact lengths L_1 – L_4 increase as a function of pressure, P , interface friction, material characteristic, and polygon geometry, up to the forming limit of the material, where failure occurs. We will therefore divide the deforming tube into segments, namely, a contact segment referred to as a linear section denoted by L , and non-contact segments referred to as free sections, which are arcs that define the radius of the part.

The following major assumptions are used in this study:

- The tube is homogeneous and isotropic.
- The elastic deformation is negligible and flow stress of the material follows the power law.
- The polygon part to be hydroformed is considered to be long enough such that the plane strain condition holds.
- The deformation of the tube is subdivided into linear and free expansion segments.
- The deformed shape of free expansion is assumed to be an arc.
- The hoop force is continuous along the hoop direction; thus the average hoop strain is assumed to be continuous.
- The tube is subjected to bending and unbending load; thus the strain and stress are different on the outside surface and inside

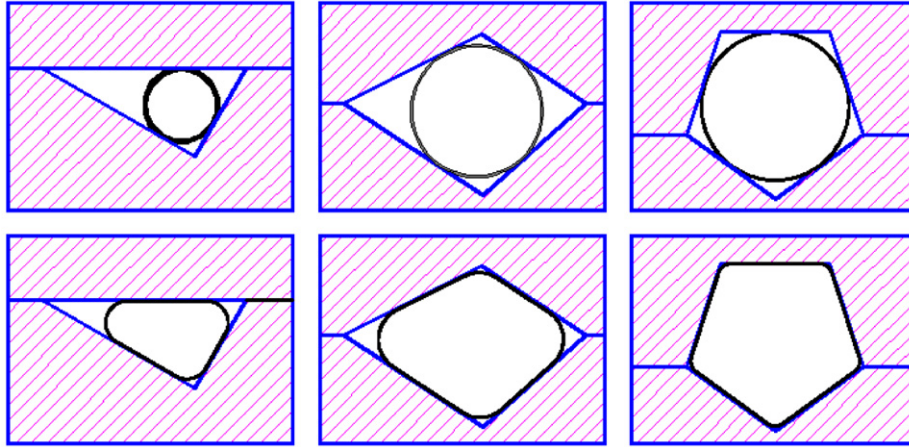


Fig. 1. Family of polygon shapes—scheme of tube hydroforming.

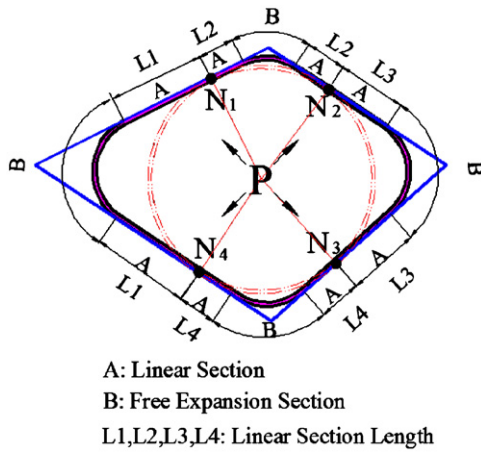


Fig. 2. Initial boundary conditions and sections in the deformed shape.

surface of the deformed tube. The tube is divided into three layers across the thickness: outside layer, neutral layer, and inside layer. The neutral layer is assumed to coincide with the middle layer of the tube.

- At the commencement of deformation, the tube should establish a contact point in each surface of the polygon.
- The friction at the tube–die interface follows Coulomb's friction law.

3.2. Preliminary analysis

Based on the above assumptions, there are two sections of different stress states along the hoop direction. In the linear section, the tube experiences bending and stretching. The outside layer of the tube is compressed relative to the neutral layer, and the inside layer is stretched relative to the neutral layer. In the free expansion section, the tube is also in the stretched state combined with bending. Bending in the free expansion zone is in the direction opposite to the bending in the linear section. Thus, the outside layer of this section is stretched relative to the neutral layer, and the inside layer is compressed relative to the neutral layer. Although the stress and strain are different through the thickness, they vary minimally through the thickness because the thickness of the tube is far smaller than the tube radius. It is therefore reasonable to assume that the variation between the hoop stress and hoop strain is approximately linear. From the above analysis, it is necessary to distinguish the stress and strain

in the respective layers. Thus the following notions are introduced in this paper.

Stress and strain in middle layer: $\varepsilon_{r,m}, \varepsilon_{\theta,m}, \varepsilon_{z,m}, \sigma_{r,m}, \sigma_{q,m}, \sigma_{z,m}$.

Stress and strain in inside layer: $\varepsilon_{r,i}, \varepsilon_{\theta,i}, \varepsilon_{z,i}, \sigma_{r,i}, \sigma_{q,i}, \sigma_{z,i}$.

Stress and strain in outside layer: $\varepsilon_{r,o}, \varepsilon_{\theta,o}, \varepsilon_{z,o}, \sigma_{r,o}, \sigma_{q,o}, \sigma_{z,o}$.

Hoop force of longitudinal unit length:

$$F_h = \int_0^t s_q dt \quad (1)$$

The stress and strain in the middle layer will be derived as average values given by the following group equations:

$$\begin{cases} \varepsilon_{\theta,ave} = \frac{\int_0^t \varepsilon_{\theta} dt}{t} = \frac{\varepsilon_{\theta,o} + \varepsilon_{\theta,i}}{2} = \varepsilon_{\theta,m} = \varepsilon_{\theta} \\ \varepsilon_{r,ave} = \frac{\int_0^t \varepsilon_r dt}{t} = \frac{\varepsilon_{r,o} + \varepsilon_{r,i}}{2} = \varepsilon_{r,m} = \varepsilon_r \\ \varepsilon_{z,ave} = \frac{\int_0^t \varepsilon_z dt}{t} = \frac{\varepsilon_{z,o} + \varepsilon_{z,i}}{2} = \varepsilon_{z,m} = \varepsilon_z \\ \sigma_{\theta,ave} = \frac{\int_0^t \sigma_{\theta} dt}{t} = \frac{\sigma_{\theta,o} + \sigma_{\theta,i}}{2} = \sigma_{\theta,m} = \sigma_{\theta} \\ \sigma_{r,ave} = \frac{\int_0^t \sigma_r dt}{t} = \frac{\sigma_{r,o} + \sigma_{r,i}}{2} = \sigma_{r,m} = \sigma_r \\ \sigma_{z,ave} = \frac{\int_0^t \sigma_z dt}{t} = \frac{\sigma_{z,o} + \sigma_{z,i}}{2} = \sigma_{z,m} = \sigma_z \end{cases} \quad (2)$$

3.3. Effective stress and effective strain—plane strain condition

Effective stress is formulated as follows:

$$\bar{\sigma} = \frac{1}{\sqrt{2}} \sqrt{(\sigma_z - \sigma_r)^2 + (\sigma_r - \sigma_{\theta})^2 + (\sigma_{\theta} - \sigma_z)^2} \quad (3)$$

Under plane strain condition where $\varepsilon_z = 0$:

$$\sigma_z = (\sigma_{\theta} + \sigma_r)/2 \quad (4)$$

Substituting Eq. (4) into Eq. (3),

$$\bar{\sigma} = \frac{\sqrt{3}}{2} \sqrt{(\sigma_q - \sigma_r)^2} \quad (5)$$

$$\bar{\sigma} = \frac{1}{\beta} (\sigma_{\theta} - \sigma_r), \quad \beta = \frac{2}{\sqrt{3}} \quad (6)$$

The effective strain is expressed in the following formula:

$$\bar{\varepsilon} = \frac{\sqrt{2}}{3} \sqrt{(\varepsilon_z - \varepsilon_r)^2 + (\varepsilon_r - \varepsilon_{\theta})^2 + (\varepsilon_{\theta} - \varepsilon_z)^2} \quad (7)$$

Due to plane strain conditions,

$$\begin{cases} \varepsilon_z = 0 \\ \varepsilon_\theta + \varepsilon_r = 0 \end{cases} \quad (8)$$

Substituting group Eq. (8) into Eq. (7), we obtain

$$\begin{aligned} \bar{\varepsilon} &= \frac{2}{\sqrt{3}} \sqrt{\varepsilon_\theta^2} \\ \bar{\varepsilon} &= \beta \varepsilon_\theta, \quad \beta = \frac{2}{\sqrt{3}} = 1.155 \end{aligned} \quad (9)$$

The power law will be used to formulate the relation between the effective stress and strain as follows:

$$\bar{\sigma} = K \bar{\varepsilon}^n \quad (10)$$

Substituting Eqs. (9) and (6) into Eq. (10), we obtain

$$\frac{1}{\beta} (\sigma_\theta - \sigma_r) = K \beta^n \varepsilon_\theta^n \quad (11)$$

$$\sigma_\theta - \sigma_r = K \beta^{n+1} \varepsilon_\theta^n \quad (12)$$

3.4. Stress and strain analysis in the linear section

3.4.1. Stress and strain analysis in middle layer of linear section

Figs. 3 and 4 show the scheme of corner-forming stress acting on an element cut from the tube. Because the equilibrium equations for all linear sections are the same, the stress state is analyzed in one corner of the tube. The only difference in the linear section is the die contact length L .

Taking summation of forces in the hoop direction we obtain

$$F_h(x + dx) - F_h(x) - \sigma_f dx = 0$$

From the definition of average hoop stress σ_θ the following equation holds:

$$\begin{cases} F_h(x) = \sigma_\theta(x)t \\ F_h(x + dx) = \sigma_\theta(x + dx)t \end{cases}$$

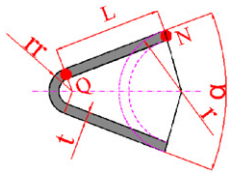


Fig. 3. Scheme of corner forming.

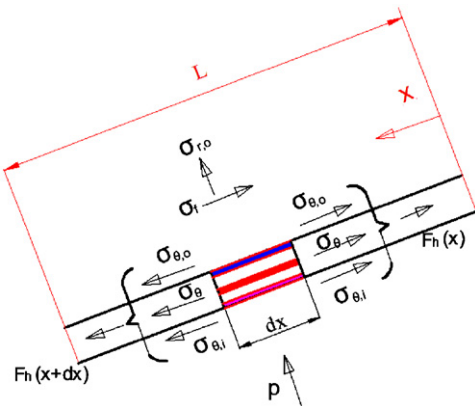


Fig. 4. Stress acting on an element.

$$\sigma_\theta(x + dx)t - \sigma_\theta(x)t - \sigma_f dx = 0$$

$$\frac{d\sigma_\theta}{dx} = \frac{1}{t} \sigma_f \quad (13)$$

$$\sigma_f = \mu |\sigma_{r,o}|$$

In the linear section, the radial stresses of three layers are the same and equal to pressure p :

$$\sigma_r = \sigma_{r,o} = \sigma_{r,i} = -p$$

Thus the following equation group represents the middle layer of a linear section:

$$\begin{cases} \frac{d\sigma_\theta}{dx} = \frac{\mu}{t} |\sigma_r| \\ -p = \sigma_r \\ \sigma_z = (\sigma_\theta + \sigma_r)/2 \end{cases} \quad (14)$$

Combining Eq. (12) with group Eq. (14), the following group of equations can be obtained:

$$\begin{cases} \frac{d\sigma_\theta}{dx} = \frac{\mu}{t} |\sigma_r| \\ -p = \sigma_r \\ \sigma_z = (\sigma_\theta + \sigma_r)/2 \\ \sigma_\theta - \sigma_r = K \beta^{n+1} \varepsilon_\theta^n \end{cases} \quad (15)$$

From equation group Eq. (15), the following group of equations can be derived:

$$\begin{cases} \sigma_\theta = K \beta^{n+1} \varepsilon_\theta^n - p \\ \frac{d\sigma_\theta}{dx} = \frac{\mu}{t} p \end{cases} \quad (16)$$

$$\frac{d\sigma_\theta}{dx} = \frac{d(K \beta^{n+1} \varepsilon_\theta^n - p)}{dx}$$

$$\frac{d\sigma_\theta}{dx} = K \beta^{n+1} n \varepsilon_\theta^{n-1} \frac{d\varepsilon_\theta}{dx} \quad (17)$$

Substituting group Eq. (16) into Eq. (17), we obtain

$$\frac{\mu}{t} p = K \beta^{n+1} n \varepsilon_\theta^{n-1} \frac{d\varepsilon_\theta}{dx} \quad (18)$$

$$t = t_0 e^{\varepsilon_\theta} = t_0 e^{-\varepsilon_\theta} \quad (19)$$

$$\frac{\mu}{t_0} e^{-\varepsilon_\theta} p = K \beta^{n+1} n \varepsilon_\theta^{n-1} \frac{d\varepsilon_\theta}{dx}$$

$$\frac{\mu}{t_0} p = K \beta^{n+1} n \varepsilon_\theta^{n-1} e^{-\varepsilon_\theta} \frac{d\varepsilon_\theta}{dx}$$

$$e^{-\varepsilon_\theta} = 1 + \sum_{i=1}^{\infty} \frac{(-1)^i (\varepsilon_\theta)^i}{i!} \quad (20)$$

$$\frac{\mu}{t_0} p = K \beta^{n+1} n \varepsilon_\theta^{n-1} \left(1 + \sum_{i=1}^{\infty} \frac{(-1)^i (\varepsilon_\theta)^i}{i!} \right) \frac{d\varepsilon_\theta}{dx}$$

$$\int \frac{\mu p}{K \beta^{n+1} n t_0} dx = \int \left(1 + \sum_{i=1}^{\infty} \frac{(-1)^i (\varepsilon_\theta)^i}{i!} \right) \varepsilon_\theta^{n-1} d\varepsilon_\theta$$

$$\frac{\mu p}{K \beta^{n+1} n t_0} x = \frac{1}{n} \varepsilon_\theta^n + \sum_{i=1}^{\infty} \frac{(-1)^i}{i!} \frac{1}{i+n} (\varepsilon_\theta)^{i+n} + C_0 \quad (21)$$

Substituting the boundary condition ($x = 0, \varepsilon_\theta = \varepsilon_N$) into Eq. (21), the constant of integration can be obtained:

$$c_0 = -\frac{1}{n} \varepsilon_N^n - \sum_{i=1}^{\infty} \frac{(-1)^i}{i!} \frac{1}{i+n} (\varepsilon_N)^{i+n} \times \frac{1}{n} (\varepsilon_\theta^n - \varepsilon_N^n) + \sum_{i=1}^{\infty} \frac{(-1)^i}{i!} \frac{1}{i+n} (\varepsilon_\theta^{i+n} - \varepsilon_N^{i+n}) = \frac{\mu p}{K \beta^{n+1} n t_0} x \quad (22)$$

After determining the average hoop strain ε_θ from Eq. (22), the remaining average stress and strain shown in the following group of equations can be computed:

$$\begin{cases} \varepsilon_r = -\varepsilon_\theta \\ \varepsilon_z = 0 \\ \sigma_\theta = K \beta^{n+1} \varepsilon_\theta^n - p \\ \sigma_r = -p \\ \sigma_z = \frac{1}{2} K \beta^{n+1} \varepsilon_\theta^n - p \end{cases} \quad (23)$$

3.4.2. Stress and strain analysis in outside layer and inside layer of linear section

In the linear section, the tube is subjected to stretching and bending. The inside layer is stretched relative to the neutral layer while the outside layer is compressed relative to the neutral layer. The hoop strain in the inside layer and outside layer can be derived from Fig. 5. Eq. (24) shows that the inside and outside hoop strain is the sum of hoop strain in the middle layer and the strain component caused by bending.

From the above figure, the following equation can be derived:

$$\begin{aligned} \varepsilon_{\theta,i} &= \ln\left(\frac{Ln'}{Li}\right) = \ln\left(\frac{e^{\varepsilon_\theta} Ln}{Li}\right) = \ln(e^{\varepsilon_\theta}) + \ln\left(\frac{Ln}{Li}\right) \\ &= \varepsilon_\theta + \ln\left(\frac{Rn}{Rn - t_0/2}\right) \\ \varepsilon_{\theta,o} &= \ln\left(\frac{Ln'}{Lo}\right) = \ln\left(\frac{e^{\varepsilon_\theta} Ln}{Lo}\right) = \ln(e^{\varepsilon_\theta}) + \ln\left(\frac{Ln}{Lo}\right) \\ &= \varepsilon_\theta + \ln\left(\frac{Rn}{Rn + t_0/2}\right) \end{aligned}$$

$$Rn = r - t_0/2$$

$$\begin{aligned} \varepsilon_{\theta,i} &= \varepsilon_\theta + \ln\left(\frac{r - t_0/2}{r - t_0}\right) = \varepsilon_\theta + \ln\left(1 + \frac{t_0/2}{r - t_0}\right) \\ \varepsilon_{\theta,o} &= \varepsilon_\theta + \ln\left(\frac{r - t_0/2}{r}\right) = \varepsilon_\theta + \ln\left(1 - \frac{t_0/2}{r}\right) \end{aligned} \quad (24)$$

Once the hoop strain in the outside and inside layers, $\varepsilon_{\theta,o}$ and $\varepsilon_{\theta,i}$, are determined, all state variables given in equation groups (25)

and (26) can be calculated.

$$\begin{cases} \varepsilon_{\theta,i} = \varepsilon_\theta + \ln\left(1 + \frac{t_0/2}{r - t_0}\right) \\ \varepsilon_{r,i} = -\varepsilon_{\theta,i} \\ \varepsilon_{z,i} = 0 \\ \sigma_{\theta,i} = K \beta^{n+1} \varepsilon_{\theta,i}^n - p \\ \sigma_{r,i} = -p \\ \sigma_{z,i} = K \beta^{n+1} \varepsilon_{\theta,i}^n / 2 - p \end{cases} \quad (25)$$

$$\begin{cases} \varepsilon_{\theta,o} = \varepsilon_\theta + \ln\left(1 - \frac{t_0/2}{r}\right) \\ \varepsilon_{r,o} = -\varepsilon_{\theta,o} \\ \varepsilon_{z,o} = 0 \\ \sigma_{\theta,o} = K \beta^{n+1} \varepsilon_{\theta,o}^n - p \\ \sigma_{r,o} = -p \\ \sigma_{z,o} = K \beta^{n+1} \varepsilon_{\theta,o}^n / 2 - p \end{cases} \quad (26)$$

3.5. Stress and strain analysis of free expansion section

3.5.1. Stress and strain analysis in middle layer of free expansion section

Throughout the free expansion section (Fig. 6), hoop force F_h is assumed to be the same along the hoop direction and equal to the hoop force at the end of linear section. This implies that average hoop stress is also uniform along the hoop direction and equal to average hoop stress at the end of linear section. The following equation group presents the stress variables, where σ_Q is the average hoop stress at the end of the linear section denoted by point Q (Fig. 6):

$$\begin{cases} \sigma_\theta = \sigma_Q \\ \sigma_r = -p/2 \\ \sigma_z = (\sigma_\theta + \sigma_r)/2 \end{cases} \quad (27)$$

Throughout the free expansion section, the average hoop strain is assumed to be the same and equal to the average hoop strain at

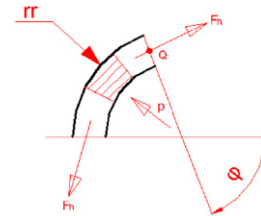


Fig. 6. Stress acting on an element in free expansion section.

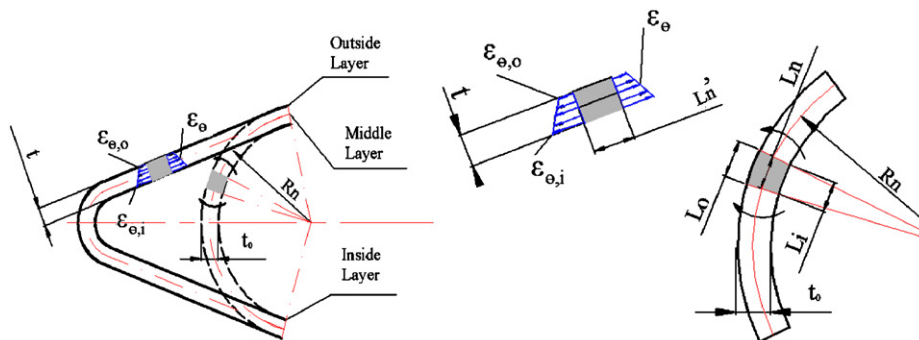


Fig. 5. Bending in the linear section.

the end of linear section.

$$\begin{cases} \varepsilon_\theta = \varepsilon_Q \\ \varepsilon_r = -\varepsilon_Q \\ \varepsilon_z = 0 \end{cases} \quad (28)$$

ε_Q can be calculated from Eq. (22) by substituting the boundary condition ($x = L, \varepsilon_\theta = \varepsilon_Q$), which gives

$$\begin{aligned} \frac{1}{n}(e_Q^n - e_N^n) + \sum_{i=1}^{\infty} \frac{(-1)^i}{i!} \frac{1}{i+n} (e_Q^{i+n} - e_N^{i+n}) \\ = \frac{\mu p}{K\beta^{n+1} n t_0} L \end{aligned} \quad (29)$$

Having determined ε_Q , all state variables in the free expansion section can be established as shown in the following group of equations:

$$\begin{cases} \varepsilon_\theta = \varepsilon_Q \\ \varepsilon_r = -\varepsilon_Q \\ \varepsilon_z = 0 \\ \sigma_\theta = K\beta^{n+1} \varepsilon_Q^n - p/2 \\ \sigma_r = -p/2 \\ \sigma_z = (\sigma_\theta + \sigma_r)/2 \end{cases} \quad (30)$$

3.5.2. Stress and strain analysis in the outside and inside layers of free expansion section

In the free expansion section, the tube is in a stretched and bending state. The inside layer is compressed, while the outside layer is stretched relative to the middle layer as shown in Fig. 7. By considering the inside and outside arc lengths of an element shown in Fig. 7, before and after deformation, the hoop strains $\varepsilon_{\theta,i}$ and $\varepsilon_{\theta,o}$ can be derived as shown below.

$$\begin{aligned} \varepsilon_{\theta,i} &= \ln\left(\frac{Li'}{Li}\right) = \ln\left(\frac{(rr-t)\omega}{(Rn-t_0/2)\varphi}\right) \\ &= \ln\left(\frac{(rr-t)Ln'/(rr-t/2)}{(Rn-t_0/2)\varphi}\right) \\ &= \ln\left(\frac{(rr-t)Ln e^{\varepsilon_\theta}/(rr-t/2)}{(Rn-t_0/2)\varphi}\right) \\ &= \ln\left(\frac{(rr-t)e^{\varepsilon_\theta} Rn \varphi/(rr-t/2)}{(Rn-t_0/2)\varphi}\right) \\ &= \ln\left(\frac{(rr-t)e^{\varepsilon_\theta} Rn/(rr-t/2)}{(Rn-t_0/2)}\right) \\ &= \ln\left(\frac{(rr-t)}{(rr-t_0/2)} e^{\varepsilon_\theta} \frac{Rn}{(Rn-t_0/2)}\right) \\ &= \varepsilon_\theta + \ln\left(\frac{(rr-t)}{(rr-t/2)} \frac{Rn}{(Rn-t_0/2)}\right) \\ &= \varepsilon_\theta + \ln\left(\frac{rr-t}{rr-t/2}\right) + \ln\left(\frac{Rn}{Rn-t_0/2}\right) \\ \varepsilon_{\theta,i} &= \varepsilon_\theta + \ln\left(\frac{rr-t_0 e^{\varepsilon_\theta}}{rr-t_0 e^{\varepsilon_\theta}/2}\right) + \ln\left(\frac{r-t_0/2}{r-t_0}\right) \end{aligned}$$

$$\begin{aligned} \varepsilon_{\theta,o} &= \ln\left(\frac{Lo'}{Lo}\right) = \ln\left(\frac{rr\omega}{(Rn-t_0/2)\varphi}\right) \\ &= \ln\left(\frac{rr(Ln'/(rr-t/2))}{(Rn+t_0/2)\varphi}\right) \\ &= \ln\left(\frac{rr(Ln e^{\varepsilon_\theta}/(rr-t/2))}{(Rn-t_0/2)\varphi}\right) \\ &= \ln\left(\frac{rr(e^{\varepsilon_\theta} Rn \varphi/(rr-t/2))}{(Rn-t_0/2)\varphi}\right) \\ &= \ln\left(\frac{rr(rr-t/2)}{(Rn-t_0/2)}\right) \\ &= \ln\left(\frac{rr}{(rr-t_0/2)} e^{\varepsilon_\theta} \frac{Rn}{(Rn+t_0/2)}\right) \\ &= \varepsilon_\theta + \ln\left(\frac{rr}{(rr-t/2)} \frac{Rn}{(Rn-t_0/2)}\right) \\ &= \varepsilon_\theta + \ln\left(\frac{rr}{rr-t/2}\right) + \ln\left(\frac{Rn}{Rn-t_0/2}\right) \\ \varepsilon_{\theta,o} &= \varepsilon_\theta + \ln\left(\frac{rr}{rr-t_0 e^{\varepsilon_\theta}/2}\right) + \ln\left(\frac{r-t_0/2}{r}\right) \end{aligned}$$

The above derivation for hoop strain in the free expansion section shows that the hoop strains in the inside and outside layers are the sum of the hoop strain in the middle layer and the strain components associated with bending. Once the hoop strain in the outside and inside layers is determined, all other state variables given in Eqs. (31) and (32) can be evaluated.

$$\begin{cases} \varepsilon_{\theta,i} = \varepsilon_\theta + \ln\left(\frac{rr-t_0 e^{\varepsilon_\theta}}{rr-t_0 e^{\varepsilon_\theta}/2}\right) + \ln\left(\frac{r-t_0/2}{r-t_0}\right) \\ \varepsilon_{r,i} = -\varepsilon_{\theta,i} \\ \varepsilon_{z,i} = 0 \\ \sigma_{\theta,i} = K\beta^{n+1} \varepsilon_{\theta,i}^n - p \\ \sigma_{r,i} = -p \\ \sigma_{z,i} = K\beta^{n+1} \varepsilon_{\theta,i}^n/2 - p \end{cases} \quad (31)$$

$$\begin{cases} \varepsilon_{\theta,o} = \varepsilon_\theta + \ln\left(\frac{rr}{rr-t_0 e^{\varepsilon_\theta}/2}\right) + \ln\left(\frac{r-t_0/2}{r}\right) \\ \varepsilon_{r,o} = -\varepsilon_{\theta,o} \\ \varepsilon_{z,o} = 0 \\ \sigma_{\theta,o} = K\beta^{n+1} \varepsilon_{\theta,o}^n \\ \sigma_{r,o} = 0 \\ \sigma_{z,o} = K\beta^{n+1} \varepsilon_{\theta,o}^n/2 \end{cases} \quad (32)$$

3.6. Prediction of deformed shape of the tube based on pressure

As a tube is hydroformed in a polygon die, the deformed tube takes the polygon shape of the die. Thus the deformed shape of the tube can be determined uniquely by the length of the linear section L related to each corner. In order to calculate the deformed shape of the tube, we need a method to calculate the length of linear section L .

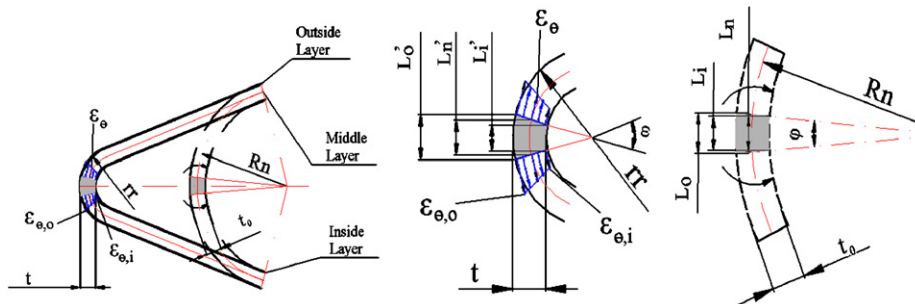


Fig. 7. Bending in the free expansion section.

The free expansion section of a deformed tube is assumed to be an arc (Fig. 6). From Eq. (30), the hoop stress in the free expansion section can be expressed by the following equation:

$$\sigma_\theta = K\beta^{n+1}\epsilon_Q^n - p/2 \quad (33)$$

Hoop stress can also be calculated by the equilibrium equation in the radial direction (Fig. 6), yielding

$$F_h - P \times rr = 0 \quad (34)$$

$$\sigma_\theta = \frac{F_h}{t} = \frac{rr}{t} p \quad (35)$$

Substituting Eqs. (19) and (35) into Eq. (33), we arrive at

$$p = \frac{K\beta^{n+1}\epsilon_Q^n t_0 e^{-\epsilon_Q}}{rr + t_0 e^{-\epsilon_Q}/2} \quad (36)$$

From Fig. 8, the following can be derived:

$$rr = r - L \operatorname{ctg}\left(\frac{\pi - \alpha}{2}\right) \quad (37)$$

$$p = \frac{K\beta^{n+1}\epsilon_Q^n t_0 e^{-\epsilon_Q}}{r - L \operatorname{ctg}(\pi - \alpha/2) + t_0 e^{-\epsilon_Q}/2} \quad (38)$$

Solving for L, Eq. (38) can be rearranged to yield

$$L = \tan\left(\frac{\pi - \alpha}{2}\right) \left(r + \frac{t_0 e^{-\epsilon_Q}}{2} - \frac{K\beta^{n+1}\epsilon_Q^n t_0 e^{-\epsilon_Q}}{p} \right) \quad (39)$$

3.7. Boundary conditions

All stress and strain in the three layers of the deformed tube can be calculated by Eqs. (22), (23), (25), (26) and (29)–(32), respectively, if the average hoop strain ϵ_N at initial contact point N is known. If the polygon die has m number of sides, then the number of initial contact points is also m (Fig. 9). From Fig. 9 if we consider pressure loading in one corner, say the corner enclosing N_1 and N_4 , we can conclude that $\epsilon_{N_1} = \epsilon_{N_4}$ and $\sigma_{N_1} = \sigma_{N_4}$. If all corners are considered, we obtain group Eq. (40) from which we can conclude that the stress and strain values of all initial contact points are the same.

$$\begin{cases} \epsilon_{N_1} = \epsilon_{N_2} & \sigma_{N_1} = \sigma_{N_2} \\ \epsilon_{N_2} = \epsilon_{N_3} & \sigma_{N_2} = \sigma_{N_3} \\ \dots & \dots \\ \epsilon_{N_{m-1}} = \epsilon_{N_m} & \sigma_{N_{m-1}} = \sigma_{N_m} \\ \epsilon_{N_m} = \epsilon_{N_{m-1}} & \sigma_{N_m} = \sigma_{N_{m-1}} \end{cases} \quad (40)$$

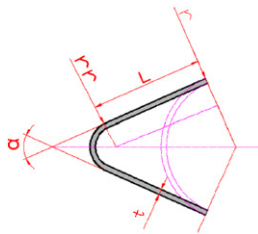


Fig. 8. Geometry relation of tube corner.

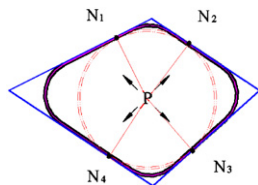


Fig. 9. Initial contact points of the tube.

The quantity of ϵ_N can be calculated by imposing a volume constant condition as follows. Before deformation, the unit volume of the tube can be expressed as

$$V_0 = \pi r^2 - \pi(r - t_0)^2 = 2\pi r t_0 - \pi t_0^2 \quad (41)$$

The unit volume after deformation can be calculated as:

$$V = \int_0^{st} t \, ds \quad (42)$$

where st is the hoop length of the deformed tube. Also,

$$V = V_0 \quad (43)$$

In order to calculate volume after deformation, the volume of corner j is calculated first (Fig. 8). Then the total volume can be obtained by summing all the volumes of all corners. In the following derivation, subscript j is added to the parameters (L_j , rr_j , $\epsilon_{Q,j}$, α_j) to denote that the parameters are related to corner j . The volume of the linear section related to corner j is calculated using the relation.

$$V_{L_j} = 2 \int_0^{L_j} t \, dx = 2 \int_0^{L_j} t_0 e^{-\epsilon_\theta} \, dx \quad (44)$$

The “ dx ” in Eq. (44) is derived from Eq. (18).

$$dx = \frac{t_0}{p\mu} K\beta^{n+1} n\epsilon_\theta^{n-1} e^{\epsilon_\theta} \, d\epsilon_\theta \quad (45)$$

Substituting Eq. (45) into Eq. (44),

$$\begin{aligned} V_{L_j} &= 2 \int_0^L t_0 e^{-\epsilon_\theta} \, dx \\ V_{L_j} &= 2 \int_{\epsilon_N}^{\epsilon_{Q,j}} t_0 e^{-\epsilon_\theta} \left\{ \frac{t_0}{p\mu} K\beta^{n+1} n\epsilon_\theta^{n-1} e^{-\epsilon_\theta} \, d\epsilon_\theta \right\} \\ V_{L_j} &= \frac{2(t_0)^2 K\beta^{n+1}}{p\mu} \int_{\epsilon_N}^{\epsilon_{Q,j}} n\epsilon_\theta^{n-1} e^{-2\epsilon_\theta} \, d\epsilon_\theta \\ e^{-2\epsilon_\theta} &= 1 + \sum_{i=1}^{\infty} \frac{(-2)^i (\epsilon_\theta)^i}{i!} \\ V_{L_j} &= \frac{2(t_0)^2 K\beta^{n+1}}{p\mu} \int_{\epsilon_N}^{\epsilon_{Q,j}} n\epsilon_\theta^{n-1} \left(1 + \sum_{i=1}^{\infty} \frac{(-2)^i (\epsilon_\theta)^i}{i!} \right) \, d\epsilon_\theta \\ V_{L_j} &= \frac{2(t_0)^2 K\beta^{n+1}}{p\mu} \int_{\epsilon_N}^{\epsilon_{Q,j}} \left(n\epsilon_\theta^{n-1} + \sum_{i=1}^{\infty} \frac{(-2)^i}{i!} n(\epsilon_\theta)^{i+n-1} \right) \, d\epsilon_\theta \\ V_{L_j} &= \frac{2(t_0)^2 K\beta^{n+1}}{p\mu} \left\{ (\epsilon_{Q,j}^n - \epsilon_N^n) + \sum_{i=1}^{\infty} \frac{(-2)^i}{i!} \frac{n}{n+i} (\epsilon_{Q,j}^{n+1} - \epsilon_N^{n+1}) \right\} \end{aligned} \quad (46)$$

The volume of the free expansion section related to corner j can be calculated as follows:

$$\begin{aligned} V_{F_j} &= \frac{(\pi - \alpha_j)}{2\pi} \{ \pi r r_j^2 - \pi (r r_j - t)^2 \} \\ V_{F_j} &= \frac{(\pi - \alpha_j)}{2\pi} \{ \pi r r_j^2 - \pi (r r_j - t_0 e^{-\epsilon_{Q,j}})^2 \} \\ V_{F_j} &= \frac{(\pi - \alpha_j)}{2} \{ 2r r_j t_0 e^{-\epsilon_{Q,j}} - (t_0 e^{-\epsilon_{Q,j}})^2 \} \end{aligned} \quad (47)$$

Substituting Eq. (37) into Eq. (47) leads to

$$V_{F_j} = \frac{(\pi - \alpha_j)}{2} \left\{ 2t_0 e^{-\epsilon_{Q,j}} \left(r - L_j \operatorname{ctg}\left(\frac{\pi - \alpha_j}{2}\right) \right) - (t_0 e^{-\epsilon_{Q,j}})^2 \right\} \quad (48)$$

The sum of the volumes of the two sections related to corner j can be expressed as.

$$V_j = V_{L_j} + V_{F_j} \quad (49)$$

Substituting Eqs. (48) and (46) into Eq. (49) yields.

$$V_j = \frac{2(t_0)^2 K \beta^{n+1}}{p \mu} \left\{ (e_{Q_j}^n - \varepsilon_N^n) + \sum_{i=1}^{\infty} \frac{(-2)^i}{i!} \frac{n}{n+i} (e_{Q_j}^{n+i} - \varepsilon_N^{n+i}) \right\} + \frac{(\pi - \alpha_j)}{2} \left\{ 2t_0 e^{-\varepsilon_{Q_j}} \left(r - L_j \operatorname{ctg} \left(\frac{\pi - \alpha_j}{2} \right) \right) - (t_0 e^{-\varepsilon_{Q_j}})^2 \right\} \quad (50)$$

The total volume of the deformed tube can be expressed as

$$V = \sum_j^m V_j \quad (51)$$

Substituting Eq. (50) into Eq. (51) yields

$$V = \sum_{j=1}^m \frac{2(t_0)^2 K \beta^{n+1}}{p \mu} \left\{ (e_{Q_j}^n - \varepsilon_N^n) + \sum_{i=1}^{\infty} \frac{(-2)^i}{i!} \frac{n}{n+i} (e_{Q_j}^{n+i} - \varepsilon_N^{n+i}) \right\} + \sum_{j=1}^m \frac{(\pi - \alpha_j)}{2} \left\{ 2t_0 e^{-\varepsilon_{Q_j}} \left(r - L_j \operatorname{ctg} \left(\frac{\pi - \alpha_j}{2} \right) \right) - (t_0 e^{-\varepsilon_{Q_j}})^2 \right\} \quad (52)$$

Substituting Eqs. (52) and (41) into Eq. (43) gives

$$2\pi r t_0 - \pi t_0^2 = \sum_{j=1}^m \frac{2(t_0)^2 K \beta^{n+1}}{p \mu} \left\{ (e_{Q_j}^n - \varepsilon_N^n) + \sum_{i=1}^{\infty} \frac{(-2)^i}{i!} \frac{n}{n+i} (e_{Q_j}^{n+i} - \varepsilon_N^{n+i}) \right\} + \sum_{j=1}^m \frac{(\pi - \alpha_j)}{2} \times \left\{ 2t_0 e^{-\varepsilon_{Q_j}} \left(r - L_j \operatorname{ctg} \left(\frac{\pi - \alpha_j}{2} \right) \right) - (t_0 e^{-\varepsilon_{Q_j}})^2 \right\} \quad (53)$$

The relationship between pressure P and the length of linear section L of each corner was given by Eq. (39). This equation is recapitulated in Eq. (54) with a subscript j representing a particular corner j .

$$L_j = \tan \left(\frac{\pi - \alpha_j}{2} \right) \left(r + \frac{t_0 e^{-\varepsilon_{Q_j}}}{2} - \frac{K \beta^{n+1} \varepsilon_{Q_j}^n t_0 e^{-\varepsilon_{Q_j}}}{p} \right) \quad (54)$$

Similarly, in a subscript form, Eq. (29) can be written as

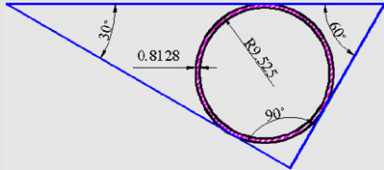
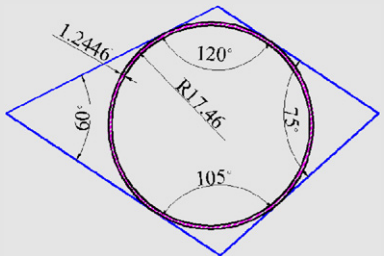
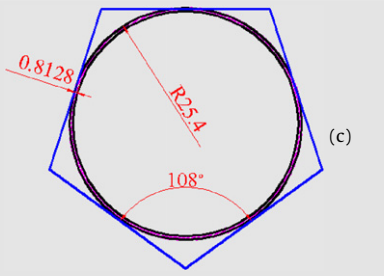
$$\frac{1}{n} (e_{Q_j}^n - \varepsilon_N^n) + \sum_{i=1}^{\infty} \frac{(-1)^i}{i!} \frac{1}{i+n} (e_{Q_j}^{i+n} - \varepsilon_N^{i+n}) = \frac{\mu p}{K \beta^{n+1} n t_0} L_j \quad (55)$$

Combining Eqs. (53)–(55), we arrived at a group equations.

$$\left\{ \begin{array}{l} L_1 = \tan \left(\frac{\pi - \alpha_1}{2} \right) \left(r + \frac{t_0 e^{-\varepsilon_{Q_1}}}{2} - \frac{K \beta^{n+1} \varepsilon_{Q_1}^n t_0 e^{-\varepsilon_{Q_1}}}{p} \right) \\ \frac{\mu p}{K \beta^{n+1} n t_0} L_1 = \frac{1}{n} (e_{Q_1}^n - \varepsilon_N^n) + \sum_{i=1}^{\infty} \frac{(-1)^i}{i!} \frac{1}{i+n} (e_{Q_1}^{i+n} - \varepsilon_N^{i+n}) \\ \dots \\ L_j = \tan \left(\frac{\pi - \alpha_j}{2} \right) \left(r + \frac{t_0 e^{-\varepsilon_{Q_j}}}{2} - \frac{K \beta^{n+1} \varepsilon_{Q_j}^n t_0 e^{-\varepsilon_{Q_j}}}{p} \right) \\ \frac{\mu p}{K \beta^{n+1} n t_0} L_j = \frac{1}{n} (e_{Q_j}^n - \varepsilon_N^n) + \sum_{i=1}^{\infty} \frac{(-1)^i}{i!} \frac{1}{i+n} (e_{Q_j}^{i+n} - \varepsilon_N^{i+n}) \\ \dots \\ L_m = \tan \left(\frac{\pi - \alpha_m}{2} \right) \left(r + \frac{t_0 e^{-\varepsilon_{Q_m}}}{2} - \frac{K \beta^{n+1} \varepsilon_{Q_m}^n t_0 e^{-\varepsilon_{Q_m}}}{p} \right) \\ \frac{\mu p}{K \beta^{n+1} n t_0} L_m = \frac{1}{n} (e_{Q_m}^n - \varepsilon_N^n) + \sum_{i=1}^{\infty} \frac{(-1)^i}{i!} \frac{1}{i+n} (e_{Q_m}^{i+n} - \varepsilon_N^{i+n}) \\ 2\pi r t_0 - \pi t_0^2 = \sum_{k=1}^m \frac{2(t_0)^2 K \beta^{n+1}}{p \mu} \left\{ (e_{Q_k}^n - \varepsilon_N^n) + \sum_{i=1}^{\infty} \frac{(-2)^i}{i!} \frac{n}{n+i} (e_{Q_k}^{n+i} - \varepsilon_N^{n+i}) \right\} \\ + \sum_{k=1}^m \frac{(\pi - \alpha_k)}{2} \left\{ 2t_0 e^{-\varepsilon_{Q_k}} \left(r - L_k \operatorname{ctg} \left(\frac{\pi - \alpha_k}{2} \right) \right) - (t_0 e^{-\varepsilon_{Q_k}})^2 \right\} \\ \dots (j = 1, 2, 3, \dots, m) \end{array} \right. \quad (56)$$

In equation group (56), there are $2m+1$ unknown variables ε_N , L_1 , L_2 , ..., L_m , ε_{Q_1} , ε_{Q_2} , ..., ε_{Q_m} . There are $2m+1$ equations in this

Table 1
Experimental parameters for tube hydroforming

Tube material	Hydroforming die geometry	Max. pressure (Mpa)
Copper (alloy122) $\phi = 19.05$ mm, $t = 0.813$ mm		27
SS 304 $\phi = 34.93$ mm, $t = 1.244$ mm	(a) Triangular polygon 	68
Copper (alloy122) $\phi = 50.8$ mm $t = 0.813$ mm	(b) Quadrilateral polygon 	48
	Pentagon	

group. These variables can therefore be determined if the internal pressure P , material property parameters K and n , friction coefficient μ and geometric dimensions r , t , α are known. The solution scheme for Eq. (56) is given in Appendix A (Table 1).

4. Validation of the analytical model

The analytical model discussed in the previous section was aimed at predicting the forming pressure, formed shape, corner fill, and wall thinning, and the stress and strain distribution for THF in regular and irregular polygon-shaped dies. In this section, hoop stress and hoop strain distribution, tube-thinning distribution, deformed shape vs pressure, and corner-fill curve obtained from the analytical model are compared with FEA simulation results and experimental results to examine the effectiveness of this analytical model. Verifications of the analytical model were carried out using three different dies: (1) triangular shaped, (2) quadrilateral shaped, and (3) pentagon shaped.

4.1. THF experiments

THF experiments were carried out using a 150-ton hydroforming test rig (Fig. 10). The test setup consists of the upper die, lower die, and two axial cylinders. The upper die is connected to a 150-ton hydraulic press through a 150-load cell. The lower die sits on a table. The dies are made of A2 steel and hardened to 62 HRC. The

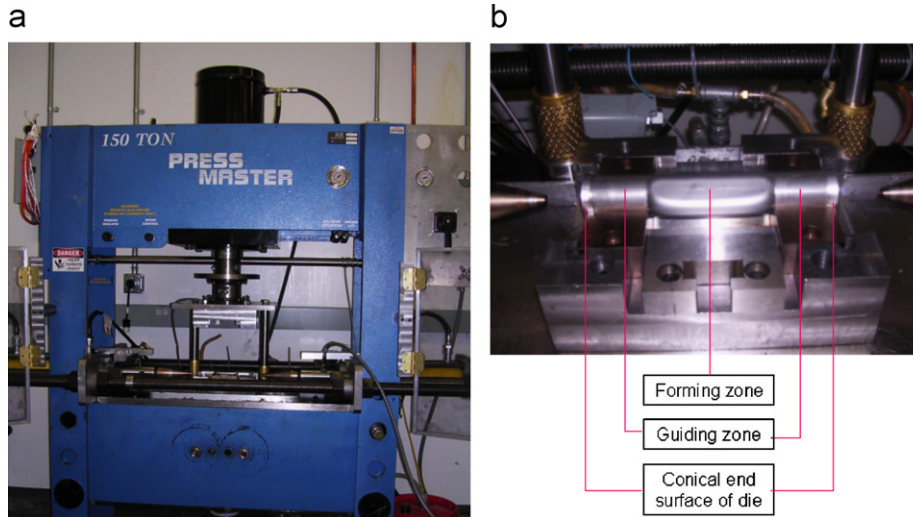


Fig. 10. Hydroforming—experimental setup: (a) 150-ton hydroforming test rig and (b) die setup.

Table 2
FEA simulation parameters and set up model

Parameters	Triangular polygon	Quadrilateral polygon	Pentagon
<i>K</i>	560 MPa	1450 MPa	560 MPa
<i>n</i>	0.46	0.6	0.46
Friction coefficient	0.05	0.05	0.1
Pressure loading	Linear increase from 0 to 40 MPa	Linear increase from 0 to 100 MPa	Linear increase from 0 to 70 MPa
<i>DYNAFORM explicit 3D-FEA</i>			
Quadrilateral shell element number	3060	2312	2226
Integration points through shell element thickness	5	5	5
Forming duration (s)	0.01	0.01	0.01
Incremental time (s)	1.2e−6	1.2e−6	1.2e−6
Mass scaling (%)	545	625	4360
Ratio of kinetic energy to internal energy (%)	Max. of 0.5	Max. of 0.8	Max. of 1.44
Tool set up FEA			
<i>ABAQUS explicit 2D-FEA</i>			
Element type	4node(CPE4R)	4node(CPE4R)	4node(CPE4R)
Element number	1114	1408	1887
Forming duration (s)	0.005	0.005	0.005
Incremental time (s)	3.40e−8S–4.25e−8S	3.68e−8S–4.27e−8S	4.56e−8S–5.31e−8S
Mass scaling (%)	100	100	100
Ratio of kinetic energy to internal energy (%)	Max. of 2.32	Max. of 3	Max. of 3.75
Tool set up FEA			

test rig has a maximum fluid pressure capacity of 140 MPa. Table 2 shows the configuration of the dies and tubular materials used for the test. Stainless-steel tubing (SS 304) and copper tubing (Alloy 122) were used. The tube length for all samples was 203.2 mm. Before testing, the dies and tubular specimens were cleaned by acetone. For each test condition, three samples were used (Fig. 11).

The specimens for triangular polygon and quadrilateral polygon were hydroformed using Teflon sheets as a lubricant. Teflon sheets 0.12 mm thick were wrapped around the specimens. The specimens for pentagon were tested using oil-based lubricant. These lubricants have friction coefficients of $\mu = 0.05$ and 0.1 for Teflon and oil-based lubricant, respectively. To emulate plane

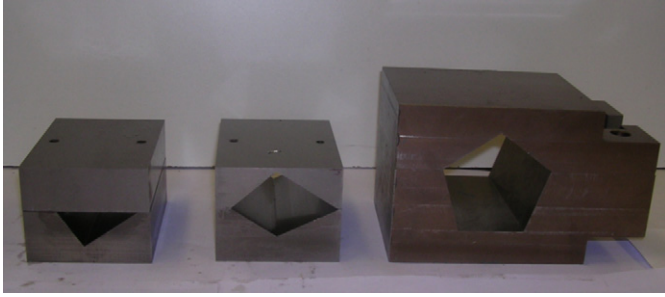


Fig. 11. Die inserts for three polygon-shaped dies.

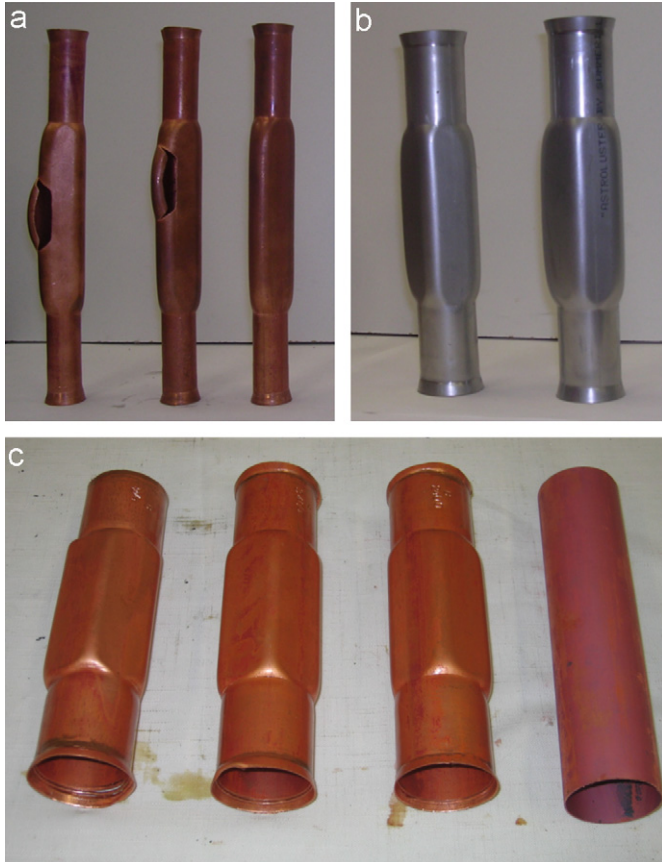


Fig. 12. Hydroformed pentagon-shaped tube: (a) triangular polygon, (b) quadrilateral polygon, and (c) pentagon.

strain conditions, the tubes were locked at the ends by forming a conical shape against a die. This conical shape also facilitated sealing of the tube. The fluid pressure was ramped linearly to the required value for 30 s. For the triangular polygon die, the maximum hydroforming pressure was 27 MPa, whereas the maximum pressure for the quadrilateral polygon was 68 MPa. For the pentagon, a maximum pressure of 48 MPa was used. Fig. 12 shows the hydroformed parts using the three different dies. After the test, the geometrical measurements of the hydroformed tubes were taken.

4.2. FE simulations

In order to verify this analytical model, 3D-FEA simulations of THF for three different polygon-shaped dies were carried

out using the commercial FEA software DYNIFORM on a PC configured with processor of 3194-MHz Pentium IV and a RAM of 2 GB. Two-dimensional plane strain FEA simulations were also carried out using ABAQUS software. FEA setup and simulation parameters are listed in Table 2. With DYNIFORM, shell elements were used to discretize the tube, and the die was treated as a rigid body. In order to approximate plane strain condition, the tube ends were fixed. In order to reduce the simulation time, mass scaling of 545%, 625% and 4360% were adopted in the simulations of triangular tube, quadrilateral tube and pentagonal, respectively, for DYNIFORM, and a mass scaling of 100% was adopted for ABAQUS 2D-plane strain simulations (Table 2).

It should be noted however that, as the level of mass scaling increases, the kinetic energy of the moving mass also increases. In order to maintain quasi-static response the recommended kinetic energy must be less than 5% of the strain energy [30]. Table 2 shows that with the adopted mass scaling, the ratio of kinetic energy to strain energy is less than 1.5% for DYNIFORM and less than 3.75% for ABAQUS simulations.

5. Results and discussion

5.1. Stress and strain distribution comparison between FEA and analysis

A comparison between analysis and FEA is given in Fig. 13 for hoop strain and hoop stress distribution pertaining to the triangular and quadrilateral polygons. The analytical model agrees well with the FEA results. Figs. 13(a) and (c) show that hoop strain on the inside of the polygon is higher at the linear sections than at the free expansion sections. In contrast, hoop strain distribution on the outside surface exhibits an opposite trend from that observed in the inside surface. As seen in Figs. 13(b) and (d), hoop stress distribution on the inside surface of the polygon exhibits the same trend as hoop strain distribution. The hoop stress and hoop strain distributions on the outside layer for the pentagon are shown in Fig. 14. It can be seen clearly that the outside surfaces of free expansion zones exhibit higher hoop strain values compared to that of the linear sections.

This alternate increase or decrease of the hoop strain and stress from the free expansion zone to the linear zone is associated with bending effects. From stress and strain analysis of the outside and inside layers, it was shown that the outside layer of the free expansion sections experiences stretching relative to the middle layer, while the inside layer experiences compression relative to the middle layer. In contrast, in the linear section the outside layer experiences compression relative to the middle layer, while the inside layer experiences stretching relative to the middle layer. Hence it can be concluded that: (i) the hoop strains and stresses on the inside layer of the linear section are higher than that on outside layer, (ii) the hoop strains and stresses on the inside layer of the free expansion sections are less than that on outside layer, (iii) when the corner radius at the free expansion section becomes small, the hoop strain components due to bending increase rapidly, which leads to rapid decrease in the hoop strain and stress on the inside layer. Thus, the hoop strain and stress on the outside layer of the free expansion section are higher than that of the linear section (Fig. 14), whereas, on the inside layer, the hoop strain and stress follow opposite trend as seen in Fig. 13.

Fig. 15 shows that the longitudinal strain distributions in the center sectional plane of triangular tube, quadrilateral tube, and pentagonal tube are less than 0.02, which is negligible comparing

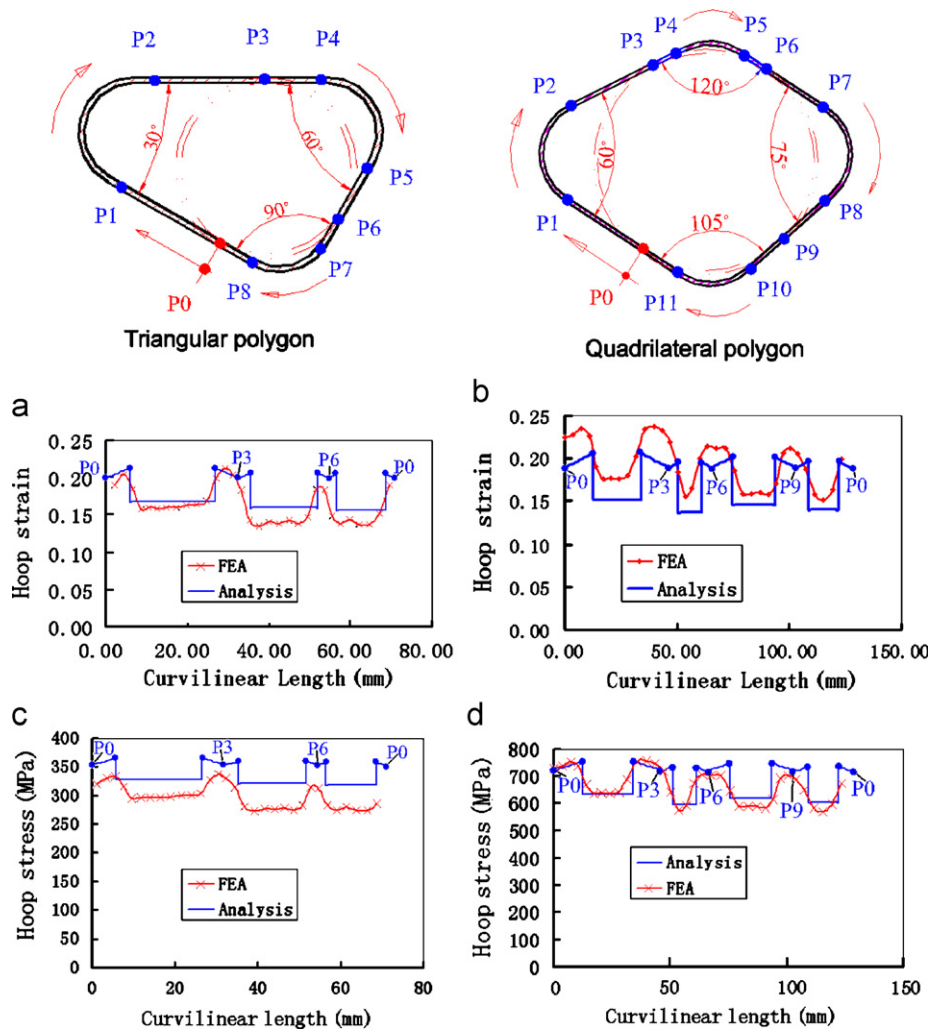


Fig. 13. Hoop stress and strain distribution comparison—analysis and DYNAFORM 3D FEA. (a) Hoop strain on inside surface, (b) hoop stress on inside surface, (c) hoop strain on inside surface, and (d) hoop stress on inside surface.

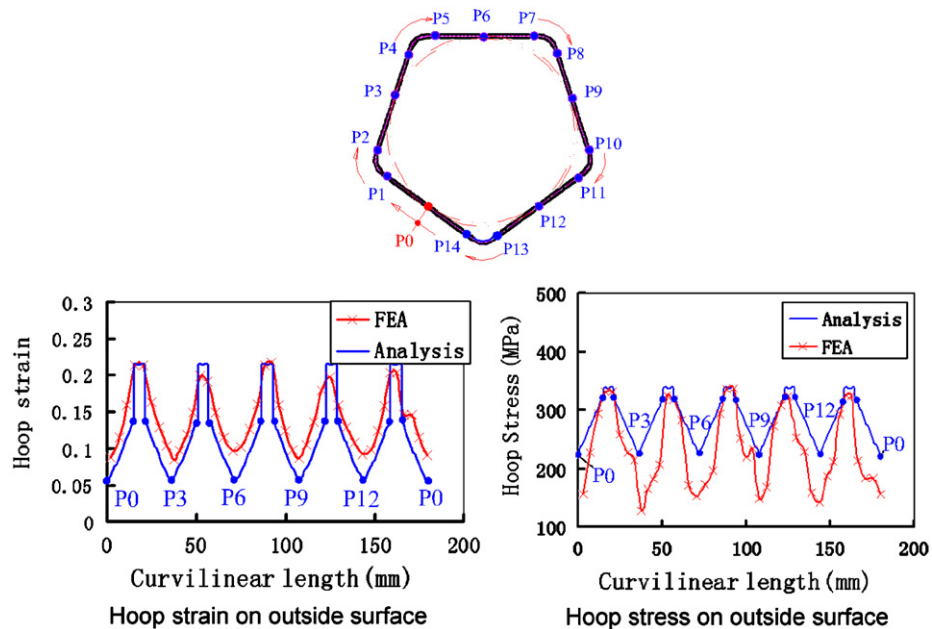


Fig. 14. Hoop strain and stress distribution comparison between analysis and DYNAFORM 3D FEA.

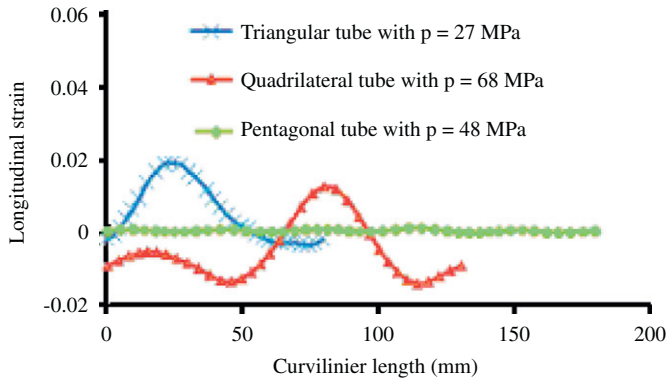


Fig. 15. Longitudinal strain distribution along the hoop direction in the center sectional plane of the tube by DYNAFORM FEA simulation.

to the hoop strains observed in Figs. 13 and 14. This shows that the plane strain condition is well approximated in the FEA simulations. Fig. 16 shows thinning rate and hoop strain comparison between 2D-plane strain FE simulations and analysis. The results show good agreement. It should be noted, however, that the hoop stress distributions from DYNAFORM were much closer to the analytical model than 2D-FEA plane strain from ABAQUS simulations.

5.2. Corner-fill, formed shape, and wall-thinning comparison—DYNAFORM FEA, experiment, and analysis

The comparison of FEA, analysis, and experiment for the deformed shape is given in Fig. 17. Figs. 17(a) and (c) show the DH1 height comparison for triangular and quadrilateral polygons obtained from experiments, analysis, and FEA. Figs. 17(b) and (d)

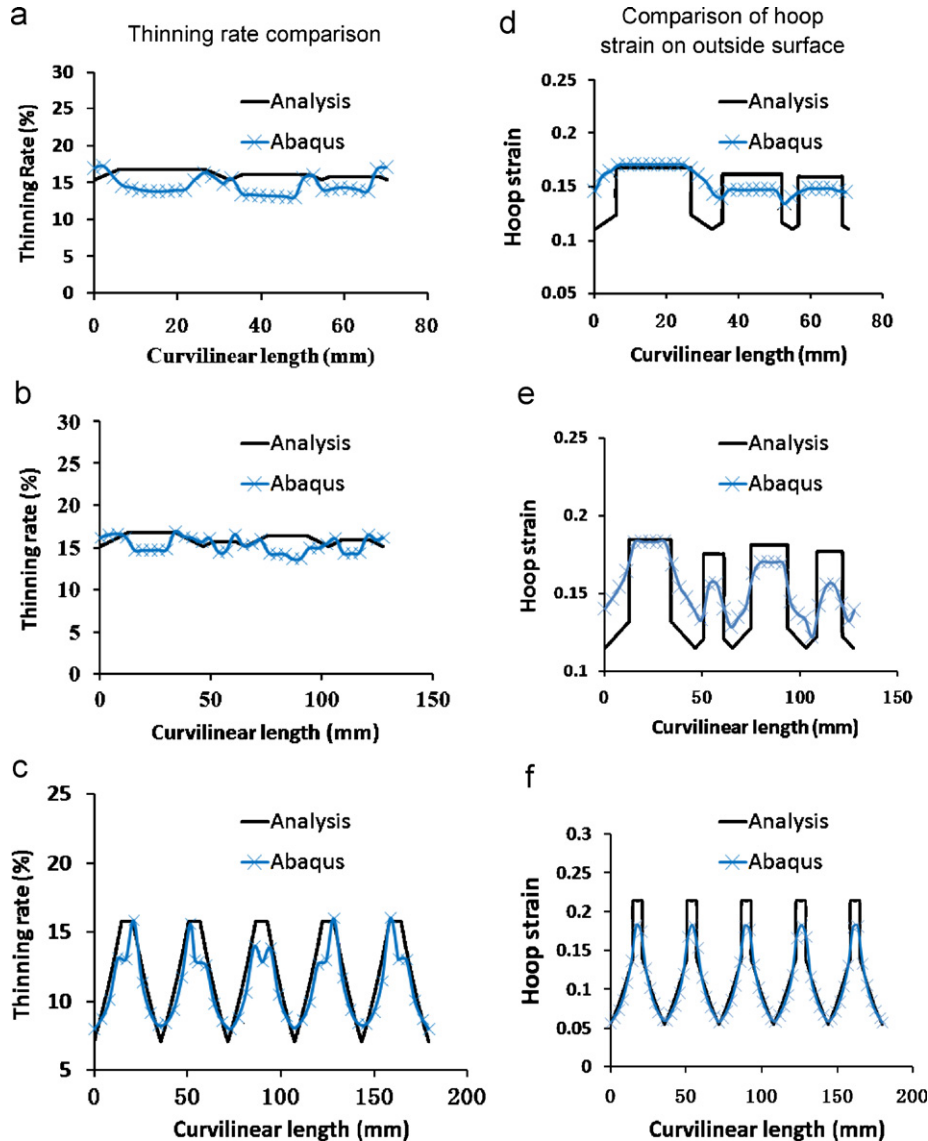


Fig. 16. Thinning and strain distribution comparison between analysis and ABAQUS 2D-FEA. (a) Thinning rate for triangular polygon, (b) thinning rate for quadrilateral polygon, (c) thinning rate for pentagon, (d) hoop strain on outside surface for triangular polygon, (e) hoop strain on outside surface for quadrilateral polygon, and (f) hoop strain on outside surface for pentagon.

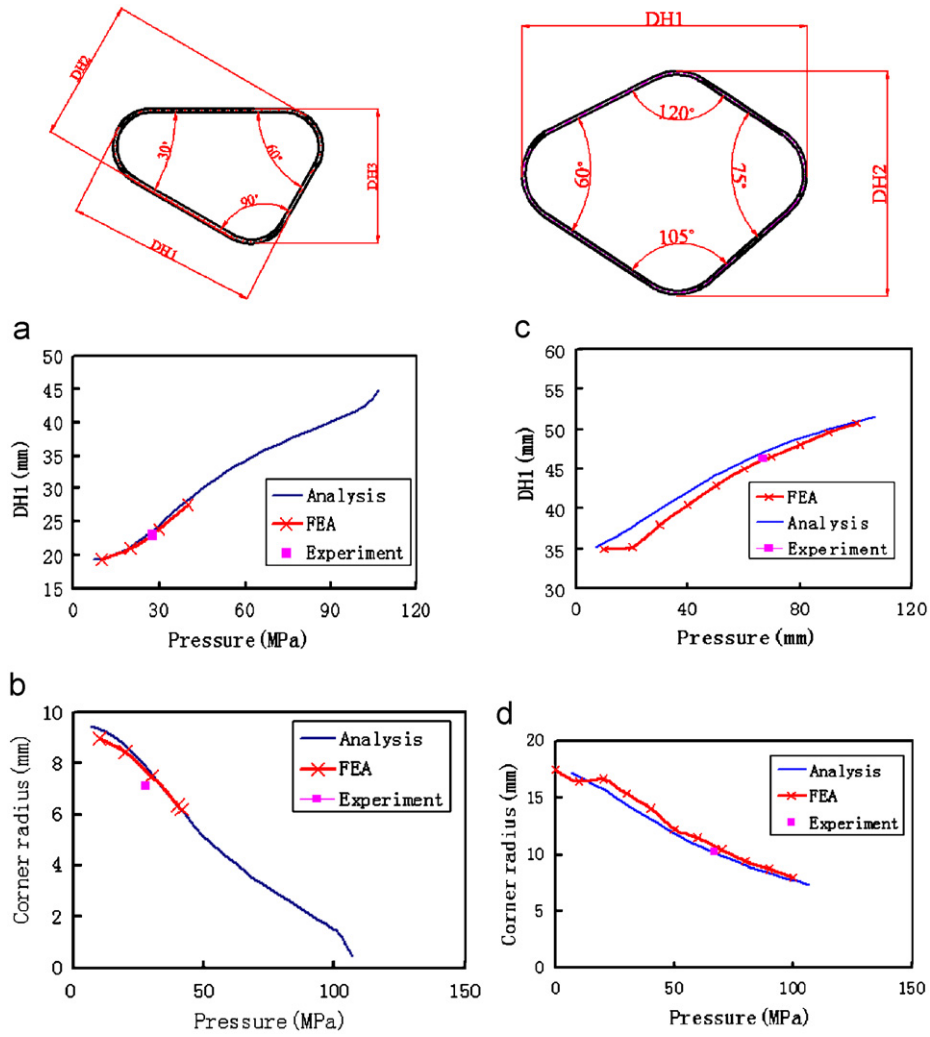


Fig. 17. Deformed shape comparison—FEA, analysis, and experiment. (a) DH1 vs pressure, (b) corner radius vs pressure (30° corner), (c) DH1 vs pressure, and (d) corner radius vs pressure (60° corner).

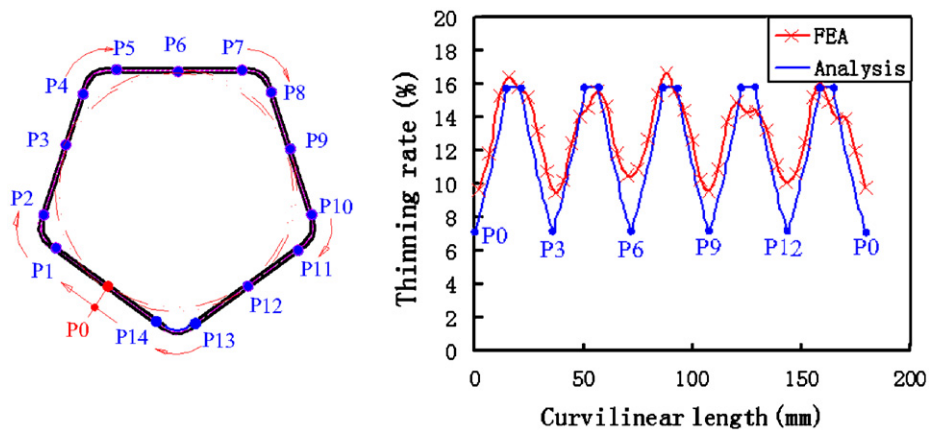


Fig. 18. Tube-thinning rate comparison between FEA and analysis.

show corner-fill profiles, where corner radius is plotted against pressure. A very good agreement among analysis, experiment, and FEA can be observed.

Fig. 18 shows the thinning rate distribution for hydroformed pentagon with good agreement between analysis and FEA. From Fig. 18, it can also be seen that the free

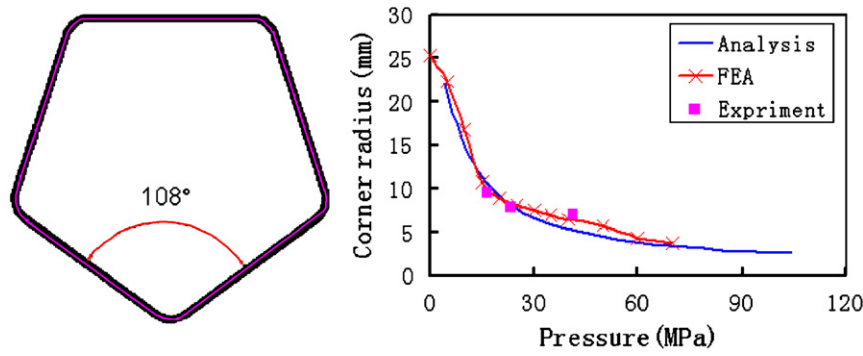


Fig. 19. Corner-fill comparison—FEA, analysis, and experiment.

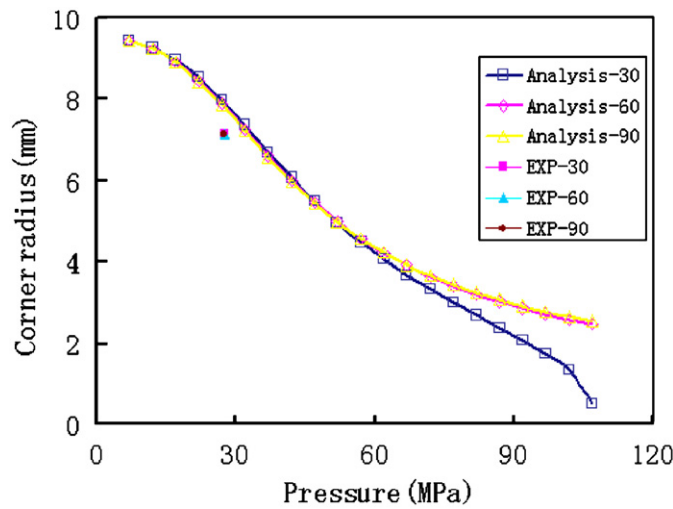
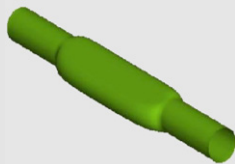
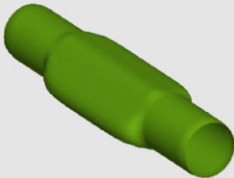
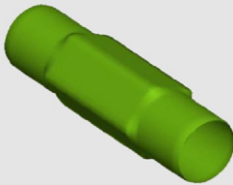

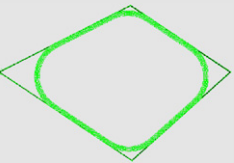
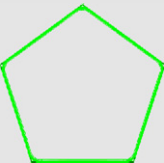


Fig. 20. Corner-fill comparison between three vertex angles (triangular polygon).

Table 3
CPU time comparison between FEA simulations and analytical model

	Triangular polygon	Quadrilateral polygon	Pentagon
DYNAFORM 3D-FEA	 At 27 MPa	 At 68 MPa	 At 48 MPa
DYNAFORM CPU time (s)	50	65	69
ABAQUS 2D-FEA	 At 27 MPa	 At 68 MPa	 At 48 MPa
ABAQUS CPU time (s)	260	373	326
Analytical modeling CPU time (s)	9.1	3.3	5.5

expansion zones experience maximum thinning. Fig. 19 shows corner-fill for 108° corner. The three experimental data points match very well with both analytical prediction and FEA (Fig. 19).

Fig. 20 shows that curves of corner radius vs pressure for different vertex angles coincide for most of the pressure range. This implies that the change in vertex angle has little influence on corner radius. This phenomenon was observed in the experi-

ments for both triangular and quadrilateral polygons. Note that both of these polygon dies have different corner angles. Fig. 20 shows that at higher pressure, the curves slightly diverge. However, this is associated with very small radii, which may not be practical.

5.3. Analytical modeling efficiency

Table 3 shows CPU time comparison between FEA simulations and analytical model. The input data for 3D-FEA simulation using DYNIFORM and 2D-plane strain simulations were discussed in Section 4.2. When compared with 3D-FEA simulations, the analytical model is 12–20 times faster than FEA analysis. Table 3 also shows that analytical model was 28–113 faster than 2D-plane strain simulations. These comparisons do not include the preprocessing time required to build the FEA models, which may take considerable amount of time. This study shows that analytical modeling can be very beneficial in studying the influence of multiple variables (parametric study) on the forming process, particularly, in the early design stages.

6. Summary and conclusions

Derivation of the analytical model for planar THF has been presented. This model can be used to predict tube hydroformed shape, corner fill, wall thinning, and hydroforming pressure. Furthermore, since the proposed model is based on deformation theory with bending effects included, stress and strain distribution across the wall thickness can be determined.

The derivation of the analytical model starts with stress and strain analysis, where the tube wall is divided into three layers: inside layer, middle layer, and outside layer. These layers experience different strain and stress levels due to combined bending and stretching. The model has been derived such that if hoop strain values are known for the inside layer, outside layer, and middle layers, then all the remaining state variables (stress and strain) can be determined. To solve the hoop strains, the boundary conditions need to be invoked. The boundary conditions include volume constancy and initial contact points whose hoop strain values are the same. The problem is solved by the Newton–Raphson method as given in Appendix A.

The analytical model was validated using FEA and THF experiments on regular and irregular polygon dies. Two materials, copper (Alloy 122) and stainless-steel (SS 304) tubing of various sizes were used. This model can be used as a quick tool to study variables of interest in THF before embarking on extensive FEA analysis, that is, the relationships involving process variables, material variables, and geometric variables can be evaluated immediately.

Acknowledgments

The authors would like to acknowledge the National Science Foundation, through which this work was funded under Project no. DMI-0448885. The authors would like to acknowledge ETA for providing the authors with DYNIFORM FEA software license, which was used to run the FE simulations.

Appendix A. Solution scheme for equation group (56)

$$\left\{ \begin{aligned} L_1 &= \tan\left(\frac{\pi - \alpha_1}{2}\right) \left(r + \frac{t_0 e^{-\epsilon_{Q,1}}}{2} - \frac{K\beta^{n+1} \epsilon_{Q,1}^n t_0 e^{-\epsilon_{Q,1}}}{p} \right) \\ \frac{\mu p}{K\beta^{n+1} n t_0} L_1 &= \frac{1}{n} (\epsilon_{Q,1}^n - \epsilon_N^n) + \sum_{i=1}^{\infty} \frac{(-1)^i}{i!} \frac{1}{i+n} (\epsilon_{Q,1}^{i+n} - \epsilon_N^{i+n}) \\ \dots &\dots \\ L_j &= \tan\left(\frac{\pi - \alpha_j}{2}\right) \left(r + \frac{t_0 e^{-\epsilon_{Q,j}}}{2} - \frac{K\beta^{n+1} \epsilon_{Q,j}^n t_0 e^{-\epsilon_{Q,j}}}{p} \right) \\ \frac{\mu p}{K\beta^{n+1} n t_0} L_j &= \frac{1}{n} (\epsilon_{Q,j}^n - \epsilon_N^n) + \sum_{i=1}^{\infty} \frac{(-1)^i}{i!} \frac{1}{i+n} (\epsilon_{Q,j}^{i+n} - \epsilon_N^{i+n}) \\ \dots &\dots \\ L_m &= \tan\left(\frac{\pi - \alpha_m}{2}\right) \left(r + \frac{t_0 e^{-\epsilon_{Q,m}}}{2} - \frac{K\beta^{n+1} \epsilon_{Q,m}^n t_0 e^{-\epsilon_{Q,m}}}{p} \right) \\ \frac{\mu p}{K\beta^{n+1} n t_0} L_m &= \frac{1}{n} (\epsilon_{Q,m}^n - \epsilon_N^n) + \sum_{i=1}^{\infty} \frac{(-1)^i}{i!} \frac{1}{i+n} (\epsilon_{Q,m}^{i+n} - \epsilon_N^{i+n}) \\ 2\pi r t_0 - \pi t_0^2 &= \sum_{k=1}^m \frac{2(t_0)^2 K\beta^{n+1}}{p\mu} \left\{ (\epsilon_{Q,k}^n - \epsilon_N^n) + \sum_{i=1}^{\infty} \frac{(-2)^i}{i!} \frac{n}{n+i} (\epsilon_{Q,k}^{n+i} - \epsilon_N^{n+i}) \right\} \\ &\quad + \sum_{k=1}^m \frac{(\pi - \alpha_k)}{2} \left\{ 2t_0 e^{-\epsilon_{Q,k}} \left(r - L_k \text{ctg}\left(\frac{\pi - \alpha_k}{2}\right) \right) - (t_0 e^{-\epsilon_{Q,k}})^2 \right\} \end{aligned} \right. \quad (j = 1, 2, 3, \dots, m) \quad (A.1)$$

Equation group (A.1) can be rearranged and divided into two equation groups (A.2) and (A.3). Equation group (A.2) consists of deformed shape prediction equations, while equation group (A.3) is derived by substituting equation group (A.2) into equation group (A.1) such that the L_1, L_2, \dots, L_m terms are eliminated. The solution for (A.1) is obtained in two steps. First, equation group (A.3) is solved to obtain $\epsilon_{Q,1}, \epsilon_{Q,2}, \dots, \epsilon_{Q,m}, \epsilon_N$. These strain variables obtained from equation group (A.3) are then substituted into equation group (A.2) to obtain L_1, L_2, \dots, L_m .

$$\left\{ \begin{aligned} L_1 &= \tan\left(\frac{\pi - \alpha}{2}\right) \left(r + \frac{t_0 e^{-\epsilon_{Q,1}}}{2} - \frac{K\beta^{n+1} \epsilon_{Q,1}^n t_0 e^{-\epsilon_{Q,1}}}{p} \right) \\ \vdots &\vdots \\ L_j &= \tan\left(\frac{\pi - \alpha}{2}\right) \left(r + \frac{t_0 e^{-\epsilon_{Q,j}}}{2} - \frac{K\beta^{n+1} \epsilon_{Q,j}^n t_0 e^{-\epsilon_{Q,j}}}{p} \right) \\ \vdots &\vdots \\ L_m &= \tan\left(\frac{\pi - \alpha}{2}\right) \left(r + \frac{t_0 e^{-\epsilon_{Q,m}}}{2} - \frac{K\beta^{n+1} \epsilon_{Q,m}^n t_0 e^{-\epsilon_{Q,m}}}{p} \right) \\ \dots (j = 1, 2, 3, \dots, m) &\dots \end{aligned} \right. \quad (A.2)$$

$$\left\{ \begin{aligned} \frac{1}{n} (\epsilon_{Q,1}^n - \epsilon_N^n) + \sum_{i=1}^{\infty} \frac{(-1)^i}{i!} \frac{1}{i+n} (\epsilon_{Q,1}^{i+n} - \epsilon_N^{i+n}) \\ - \frac{\mu p}{K\beta^{n+1} n t_0} \tan\left(\frac{\pi - \alpha}{2}\right) \left(r + \frac{t_0 e^{-\epsilon_{Q,1}}}{2} - \frac{K\beta^{n+1} \epsilon_{Q,1}^n t_0 e^{-\epsilon_{Q,1}}}{p} \right) \\ \vdots \\ \frac{1}{n} (\epsilon_{Q,j}^n - \epsilon_N^n) + \sum_{i=1}^{\infty} \frac{(-1)^i}{i!} \frac{1}{i+n} (\epsilon_{Q,j}^{i+n} - \epsilon_N^{i+n}) \\ - \frac{\mu p}{K\beta^{n+1} n t_0} \tan\left(\frac{\pi - \alpha}{2}\right) \left(r + \frac{t_0 e^{-\epsilon_{Q,j}}}{2} - \frac{K\beta^{n+1} \epsilon_{Q,j}^n t_0 e^{-\epsilon_{Q,j}}}{p} \right) \\ \vdots \\ \frac{1}{n} (\epsilon_{Q,m}^n - \epsilon_N^n) + \sum_{i=1}^{\infty} \frac{(-1)^i}{i!} \frac{1}{i+n} (\epsilon_{Q,m}^{i+n} - \epsilon_N^{i+n}) \\ - \frac{\mu p}{K\beta^{n+1} n t_0} \tan\left(\frac{\pi - \alpha}{2}\right) \left(r + \frac{t_0 e^{-\epsilon_{Q,m}}}{2} - \frac{K\beta^{n+1} \epsilon_{Q,m}^n t_0 e^{-\epsilon_{Q,m}}}{p} \right) \\ \frac{\sum_{k=1}^m \frac{2(t_0)^2 K\beta^{n+1}}{p\mu} \left\{ (\epsilon_{Q,k}^n - \epsilon_N^n) + \sum_{i=1}^{\infty} \frac{(-2)^i}{i!} \frac{n}{n+i} (\epsilon_{Q,k}^{n+i} - \epsilon_N^{n+i}) \right\}}{+ \sum_{k=1}^m \frac{(\pi - \alpha)}{2} \left\{ 2t_0 e^{-\epsilon_{Q,k}} \left(r - L_j \text{ctg}\left(\frac{\pi - \alpha}{2}\right) \right) - (t_0 e^{-\epsilon_{Q,k}})^2 \right\}} \end{aligned} \right. = \begin{aligned} &0 \\ &0 \\ &0 \\ &0 \\ &2\pi r t_0 - \pi t_0^2 \end{aligned} \quad \dots (j = 1, 2, 3, \dots, m) \quad (A.3)$$

Equation group (A.3) can be solved by Newton–Raphson method as follows:

(1) Reform the equation group (A.3) into the following equation group:

$$F = \begin{cases} f_1 \\ \vdots \\ f_j \\ \vdots \\ f_m \\ f_{m+1} \end{cases} = \begin{cases} \frac{1}{n}(e_{Q,1}^n - e_N^n) + \sum_{i=1}^{\infty} \frac{(-1)^i}{i!} \frac{1}{i+n} (e_{Q,1}^{i+n} - e_N^{i+n}) \\ - \frac{\mu p}{K\beta^{n+1} n t_0} \tan\left(\frac{\pi - \alpha}{2}\right) \left(r + \frac{t_0 e^{-\epsilon_{Q,1}}}{2} - \frac{K\beta^{n+1} e_{Q,1}^n t_0 e^{-\epsilon_{Q,1}}}{p} \right) \\ \vdots \\ \frac{1}{n}(e_{Q,j}^n - e_N^n) + \sum_{i=1}^{\infty} \frac{(-1)^i}{i!} \frac{1}{i+n} (e_{Q,j}^{i+n} - e_N^{i+n}) \\ - \frac{\mu p}{K\beta^{n+1} n t_0} \tan\left(\frac{\pi - \alpha}{2}\right) \left(r + \frac{t_0 e^{-\epsilon_{Q,j}}}{2} - \frac{K\beta^{n+1} e_{Q,j}^n t_0 e^{-\epsilon_{Q,j}}}{p} \right) \\ \vdots \\ \frac{1}{n}(e_{Q,m}^n - e_N^n) + \sum_{i=1}^{\infty} \frac{(-1)^i}{i!} \frac{1}{i+n} (e_{Q,m}^{i+n} - e_N^{i+n}) \\ - \frac{\mu p}{K\beta^{n+1} n t_0} \tan\left(\frac{\pi - \alpha}{2}\right) \left(r + \frac{t_0 e^{-\epsilon_{Q,m}}}{2} - \frac{K\beta^{n+1} e_{Q,m}^n t_0 e^{-\epsilon_{Q,m}}}{p} \right) \\ f_{m+1} = \sum_{k=1}^m \frac{2(t_0)^2 K\beta^{n+1}}{p\mu} \left\{ (e_{Q,k}^n - e_N^n) + \sum_{i=1}^{\infty} \frac{(-2)^i}{i!} \frac{n}{n+i} (e_{Q,k}^{n+i} - e_N^{n+i}) \right\} \\ + \sum_{k=1}^m \frac{(\pi - \alpha)}{2} \left\{ 2t_0 e^{-\epsilon_{Q,k}} \left(r - L_j \operatorname{ctg}\left(\frac{\pi - \alpha}{2}\right) \right) - (t_0 e^{-\epsilon_{Q,k}})^2 \right\} - 2\pi r t_0 - \pi t_0^2 \end{cases} \dots (j = 1, 2, 3, \dots, m) \tag{A.4}$$

(2) Get the Jacobian matrix of F

$$Df(\epsilon_{Q,1}, \dots, \epsilon_{Q,m}, \epsilon_N) = \begin{bmatrix} \frac{\partial f_1}{\partial \epsilon_{Q,1}} & \dots & \frac{\partial f_1}{\partial \epsilon_{Q,i}} & \dots & \frac{\partial f_1}{\partial \epsilon_{Q,m}} & \frac{\partial f_1}{\partial \epsilon_N} \\ \frac{\partial f_2}{\partial \epsilon_{Q,1}} & \dots & \frac{\partial f_2}{\partial \epsilon_{Q,i}} & \dots & \frac{\partial f_2}{\partial \epsilon_{Q,m}} & \frac{\partial f_2}{\partial \epsilon_N} \\ \vdots & \vdots & \vdots & \vdots & \vdots & \vdots \\ \frac{\partial f_j}{\partial \epsilon_{Q,1}} & \dots & \frac{\partial f_j}{\partial \epsilon_{Q,i}} & \dots & \frac{\partial f_j}{\partial \epsilon_{Q,m}} & \frac{\partial f_j}{\partial \epsilon_N} \\ \vdots & \vdots & \vdots & \vdots & \vdots & \vdots \\ \frac{\partial f_{m+1}}{\partial \epsilon_{Q,1}} & \dots & \frac{\partial f_{m+1}}{\partial \epsilon_{Q,i}} & \dots & \frac{\partial f_{m+1}}{\partial \epsilon_{Q,m}} & \frac{\partial f_{m+1}}{\partial \epsilon_N} \end{bmatrix}$$

(3) Assign initial guess to these unknown variables $(\epsilon_{Q,1}, \dots, \epsilon_{Q,m}, \epsilon_N)$ as

$$\begin{bmatrix} \epsilon_{Q,1} \\ \vdots \\ \epsilon_{Q,j} \\ \vdots \\ \epsilon_{Q,m} \\ \epsilon_N \end{bmatrix}_k$$

(4) Obtain $(\epsilon_{Q,1}, \dots, \epsilon_{Q,j}, \dots, \epsilon_{Q,m})$ by iterating the following:

$$\begin{bmatrix} \epsilon_{Q,1} \\ \vdots \\ \epsilon_{Q,j} \\ \vdots \\ \epsilon_{Q,m} \\ \epsilon_N \end{bmatrix}_{k+1} = \begin{bmatrix} \epsilon_{Q,1} \\ \vdots \\ \epsilon_{Q,j} \\ \vdots \\ \epsilon_{Q,m} \\ \epsilon_N \end{bmatrix}_k + Df(\epsilon_{Q,1}, \dots, \epsilon_{Q,m}, \epsilon_N)_k^{-1} \begin{bmatrix} f_1 \\ \vdots \\ f_j \\ \vdots \\ f_m \\ f_{m+1} \end{bmatrix}_k \tag{A.6}$$

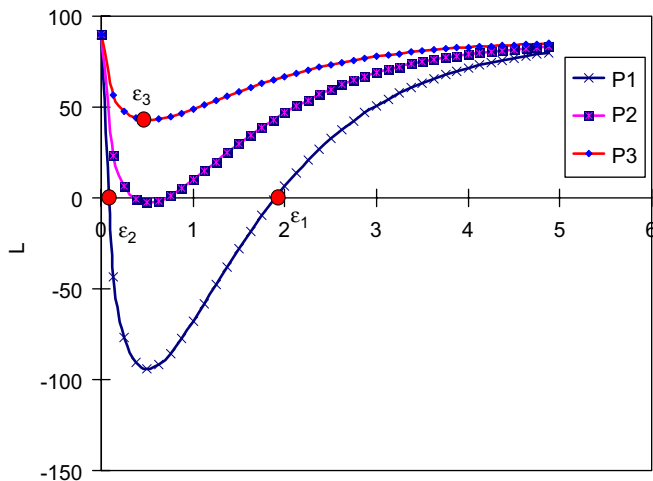


Fig. A1. Curves of L vs ϵ_Q .

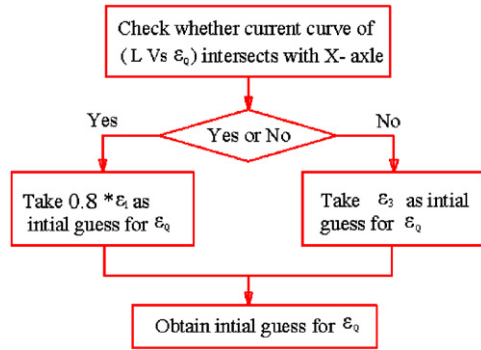


Fig. A2. Algorithm of initial guess of ε_Q .

(5) When $\|F\| < \text{error}$, stop the iterations.

In step 3, initial guess should be provided for the first iteration. In order to obtain a reasonable initial guess for $\varepsilon_{Q1}, \varepsilon_{Q2}, \dots, \varepsilon_{Qm}$, we first study the characteristics of deformed shape prediction equation by substituting $K = 500$, $n = 0.5$, $\beta = 1.15$, $\alpha = 60$, $r = 50$, $t_0 = 2$, and $P1 = 20$, $P2 = 40$, $P3 = 80$ into Eq. (A.7), which gives three curves of $(L \text{ vs } \varepsilon_Q)$ shown in Fig. A1. From Fig. A1, it can be observed that L initially decreases with increase of ε_Q to a minimum value and start increasing with increase of ε_Q . L may sometimes become negative. The initial guesses that lead to negative L should be avoided. For example, initial guess between ε_1 and ε_2 shown in Fig. A1 should be avoided. Fig. A2 shows an effective algorithm to provide a reasonable initial guess for ε_Q .

$$L = \tan\left(\frac{\pi - \alpha}{2}\right) \left(r + \frac{t_0 e^{-\varepsilon_Q}}{2} - \frac{K \beta^{n+1} \varepsilon_Q^n t_0 e^{-\varepsilon_Q}}{p} \right) \quad (\text{A.7})$$

References

- [1] Altan T, Jain N, Shi X, Ngaile G. Progressive die sequence design for deep drawing round cups using finite element analysis. *ASME Journal of Manufacturing* 2006;128:336–69.
- [2] Jirathearanat S. Advanced methods for finite element simulation of part and process design in tube hydroforming. PhD dissertation, Ohio State University, 2004.
- [3] Strano M, Jirathearanat S, Altan T. Adaptive FEM simulation: a geometric-based for wrinkle detection. *CIRP Annals—Manufacturing Technology* 2001;50(1):185–90.
- [4] Aue-U-Lan Y, Ngaile G, Altan T. Optimizing tube hydroforming using process simulation and experimental verification. *Journal of Materials Processing Technology* 2004;146:137–43.
- [5] Jirathearanat S, Hartl C, Altan T. Hydroforming of Y-shapes—product and process design using FEA simulation and experiments. *Journal of Materials Processing Technology* 2004;146:124–9.
- [6] Ray P, Mac Donald BJ. Determination of the optimal load path for tube hydroforming processes using a fuzzy load control algorithm and finite element analysis. *Finite Elements in Analysis and Design* 2004;41:173–92.
- [7] Lin FC, Kwan CT. Application of abductive network and FEM to predict an acceptable product on T-shape tube hydroforming process. *Computers and Structures* 2004;82:1189–200.
- [8] Gao L, Motsch S, Strano M. Classification and analysis of tube hydroforming processes with respect to adaptive FEM simulations. *Journal of Materials Processing Technology* 2002;129:261–7.
- [9] Yang J, Jeon B, Oh S. Design sensitivity analysis and optimization of the hydroforming processes. *Journal of Materials Processing Technology* 2001;113:666–72.
- [10] Asnafi N. Analytical modeling of tube hydroforming. *Thin-Walled Structures* 1999;34:295–330.
- [11] Xia Z. Failure analysis of tubular hydroforming. *ASME Journal of Engineering Materials and Technology* 2001;123:423–9.
- [12] Koc M, Altan T. Prediction of forming limits and parameters in the tube hydroforming process. *International Journal of Machine Tools and Manufacture* 2002;42:123–38.
- [13] Nefussi G, Combesure A. Coupled buckling and plastic instability for tube hydroforming. *International Journal of Mechanical Sciences* 2002;44(5):899–914.
- [14] Song WJ, Kim SW, Kim J, Kang BS. Analytical and numerical analysis of bursting failure prediction in tube hydroforming. *Journal of Materials Processing Technology* 2005;164–165:1618–23.
- [15] Jain N, Wang J, Alexander R. Finite element analysis of dual hydroforming processes. *Journal of Materials Processing Technology* 2004;145(1):59–65.
- [16] Rama SC, Ma K, Smith LM, Zhang JM. Two dimensional approach for simulation of hydroforming expansion of tubular cross-section without axial feed. *Journal of Materials Processing Technology* 2003;141:420–30.
- [17] Chen JY, Xia ZC, Tang SC. Corner fill modeling of tube hydroforming. In: *Proceeding of the ASME, MED*, vol. 11; 2000. p. 635–40.
- [18] Kridli GT, Bao L, Mallick PK, Tian Y. Investigation of thickness variation and corner filling in tube hydroforming. *Journal of Materials Processing Technology* 2003;133:287–96.
- [19] Liu G, Yuan S, Teng B. Analysis of thinning at the transition corner in tube hydroforming. *Journal of Materials Processing Technology* 2006;177:688–91.
- [20] Hwang YM, Chen WC. Analysis and finite element simulation of tube expansion in a rectangular cross-sectional die. In: *Proceedings of the Institution of Mechanical Engineers, Part B: Journal of Engineering Manufacture* 2003;217:127–35.
- [21] Hwang YM, Chen WC. Analysis of tube hydroforming in a square cross-sectional die. *International Journal of Plasticity* 2005;21:1815–33.
- [22] Orban H, Hu SJ. Analytical modeling of wall thinning during corner filling in structural tube hydroforming. *Journal of Materials Processing Technology* 2007;194:7–14.
- [23] Miller JE, Kyriakides S, Bastard AH. On bend–stretch forming of aluminum extruded tubes I: experiments. *International Journal of Mechanical Sciences* 2001;43:1283–317.
- [24] Miller JE, Kyriakides S, Corona E. On bend–stretch forming of aluminum extruded tubes II: analysis. *International Journal of Mechanical Sciences* 2001;43:1319–38.
- [25] Corona E. A simple analysis for bend–stretch forming of aluminum extrusions. *International Journal of Mechanical Sciences* 2004;46:433–48.
- [26] Guan Y, Pourboghrat F. Fourier series based finite element analysis of tube hydroforming—generalized plane strain model. *Journal of Materials Processing Technology* 2008;197:379–92.
- [27] Guan Y, Pourboghrat F, Yu W. Fourier series based finite element analysis of tube hydroforming—an axisymmetric model. *Engineering Computations* 2006;23(7):697–728.
- [28] Smith LM, Caveney JJ, Sun T. Fundamental concepts for corner forming limit diagrams and closed-form formulas for planar tube hydroforming analysis. *Journal of Manufacturing Science and Engineering* 2006;128:874–83.
- [29] Smith LM, Sun T. A non-finite element approach for tubular hydroforming simulation featuring a new sticking friction model. *Journal of Materials Processing Technology* 2006;171:214–22.
- [30] Prior AM. Applications of implicit and explicit finite element techniques to metal forming. *Journal of Materials Processing Technology* 1994;45:649–56.